Fall 2014

Solid oxide fuel cell electrolytes produced via very low pressure suspension plasma spray and electrophoretic deposition

James D Fleetwood
Purdue University

Recommended Citation

Fleetwood, James D, "Solid oxide fuel cell electrolytes produced via very low pressure suspension plasma spray and electrophoretic deposition" (2014). *Open Access Dissertations*. 267.
https://docs.lib.purdue.edu/open_access_dissertations/267

Graduate School Form 30
(Updated 11/20/2014)

PURDUE UNIVERSITY
GRADUATE SCHOOL
Thesis/Dissertation Acceptance

This is to certify that the thesis/dissertation prepared

By James D. Fleetwood

Entitled
Solid Oxide Fuel Cell Electrolytes Produced via Very Low Pressure Suspension Plasma Spray and Electrophoretic Deposition

For the degree of Doctor of Philosophy

Is approved by the final examining committee:

Rodney Trice	Elliott Slamovich
Eric Kvam	Kevin Trumble

To the best of my knowledge and as understood by the student in the Thesis/Dissertation Agreement, Publication Delay, and Certification/Disclaimer (Graduate School Form 32), this thesis/dissertation adheres to the provisions of Purdue University's "Policy on Integrity in Research" and the use of copyrighted material.

Approved by Major Professor(s): Rodney Trice
~~Elliott Slamovich~~

Approved by: David Bahr 12/05/2014

Head of the Department Graduate Program Date

SOLID OXIDE FUEL CELL ELECTROLYTES PRODUCED VIA VERY LOW PRESSURE SUSPENSION PLASMA SPRAY AND ELECTROPHORETIC DEPOSITION

A Dissertation
Submitted to the Faculty
of
Purdue University
by
James D. Fleetwood

In Partial Fulfillment of the
Requirements for the Degree
of
Doctor of Philosophy

December 2014
Purdue University
West Lafayette, Indiana

ACKNOWLEDGEMENTS

The author would like to thank Dr. Patricia Metcalf of Purdue University for her help with laboratory equipment, as well as Francoise Anguoa and Kent VanEvery for their work on SOFC testing and suspension plasma spray, respectively. James McCloskey, Dr. Aaron Hall, Marlene Knight, and Dave Urrea were all very helpful at the Thermal Spray Research Laboratory. Finally, the advice of Prof. Rodney Trice, Prof. Elliott Slamovich, and Dr. Aaron Hall in deciding the direction of this research was most valuable.

CONTENTS

Page

LIST OF TABLES

Table Page

Table Page

LIST OF FIGURES

Figure Page

Figure Page

NOMENCLATURE

DOE	Department of Energy
SNL	Sandia National Laboratories
TSRL	Thermal Spray Research Laboratory
NASA	National Aeronautics and Space Administration
SOFC	Solid Oxide Fuel Cell
SPS	Suspension Plasma Spray
VLPPS	Very Low Pressure Plasma Spray
VLPSPS	Very Low Pressure Suspension Plasma Spray
YSZ	Yttria Stabilized Zirconia
GDC	Gadolinia Doped Ceria
SEM	Scanning Electron Microscopy
EDS	Energy Dispersive Spectroscopy
XRD	X-ray Diffraction
EPD	Electrophoretic Deposition

ABSTRACT

Fleetwood, James D. Ph.D., Purdue University, December 2014. Solid Oxide Fuel Cell Electrolytes Produced via Very Low Pressure Suspension Plasma Spray and Electrophoretic Deposition. Major Professors: Rodney W. Trice and Elliott Slamovich, School of Materials Engineering.

Solid oxide fuel cells (SOFCs) are a promising element of comprehensive energy policies due to their direct mechanism for converting the oxidization of fuel, such as hydrogen, into electrical energy. Both very low pressure plasma spray and electrophoretic deposition allow working with high melting temperature SOFC suspension based feedstock on complex surfaces, such as in non-planar SOFC designs. Dense, thin electrolytes of ideal composition for SOFCs can be fabricated with each of these processes, while compositional control is achieved with dissolved dopant compounds that are incorporated into the coating during deposition. In the work reported, sub-micron 8 mole % Y_2O_3-ZrO_2 (YSZ) and gadolinia-doped ceria (GDC), powders, including those in suspension with scandium-nitrate dopants, were deposited on NiO-YSZ anodes, via very low pressure suspension plasma spray (VLPSPS) at Sandia National Laboratories' Thermal Spray Research Laboratory and electrophoretic deposition (EPD) at Purdue University.

Plasma spray was carried out in a chamber held at 320 - 1300 Pa, with the plasma composed of argon, hydrogen, and helium. EPD was characterized utilizing constant current deposition at 10 mm electrode separation, with deposits sintered from 1300 – 1500 °C for 2 hours. The role of suspension constituents in EPD was analyzed based on a parametric study of powder loading, powder specific surface area, polyvinyl butyral (PVB) content, polyethyleneimine (PEI) content, and acetic acid content. Increasing PVB content and reduction of particle specific surface area were found to eliminate the formation of cracks when drying. PEI and acetic acid content were used to control suspension stability and the adhesion of deposits. Additionally, EPD was used to fabricate YSZ/GDC bilayer electrolyte systems. The resultant YSZ electrolytes were 2-27 microns thick and up to 97% dense. Electrolyte performance as part of a SOFC system with screen printed LSCF cathodes was evaluated with peak power densities as high as 520 mW/cm^2 at 800 °C for YSZ and 350 mW/cm^2 at 800 °C for YSZ/GDC bilayer electrolytes.

CHAPTER 1. INTRODUCTION

1.1 Motivation for Solid Oxide Fuel Cell Research

Worldwide energy problems are alarming because there is an ongoing rise in demand for energy coupled with simultaneous and continued depletion of energy resources. The solution to this energy crisis will require every available energy technology, including nuclear, solar, wind, clean burning coal, and hydrogen. Solid oxide fuel cells (SOFCs), which can be powered by hydrogen, are a promising part of the solution because they provide a direct mechanism for converting the oxidization of fuel into electrical energy. They have a relatively simple design, conducive to durability and longevity. Essentially, oxygen in the form of air is supplied to a cathode where O^{2-} is catalyzed, which diffuses through an oxygen conducting electrolyte to the anode. Fuel, in the form of hydrogen is supplied to the anode where hydrogen reacts with O^{2-} to form H_2O, releasing electrons to complete the circuit. Advantages of SOFCs include increased efficiency, no moving parts of traditional competing technologies, no expensive platinum catalysts, and decreased emission of SO_x and NO_x.

Despite success developing SOFCs in the past 15+ years, there is still need for improvement of current SOFC technology, particularly electrolyte materials. The ideal electrolyte is: (1) applied easily to non-planar shapes to take advantage of tubular SOFC designs, (2) both pore free and thin (<50 µm), and (3) has a large oxygen ion conductivity.

1.2 Solid Oxide Fuel Cells (SOFCs)

Solid oxide fuel cells (SOFCs) are a type of hydrogen fuel cell in which the anode, electrolyte, and cathode are composed of oxide ceramics. SOFCs can achieve efficiencies of 65%, with higher efficiencies available in cogeneration systems, such as when combined with turbine engines [1]. A diagram of hydrogen fuel cell operation can be seen in Figure 1. During hydrogen fuel cell operation, O_2 is first reduced at the cathode. It then diffuses through the electrolyte and oxidizes the H_2 at the anode, creating H_2O [1,2]. The electrolyte must be gas impermeable and conduct only the oxygen ions, not electrons. This separates the electrochemical reactions, forcing the electrons to travel in a circuit between the electrodes, allowing for power generation. The electrode materials are both electronically and ionically conductive, while also serving to catalyze H_2 oxidation at the anode and O_2 reduction at the cathode [1]. The Nernst equation, seen in Equation 1, describes the electrochemical potential between the cathode and anode, where R is the gas constant, 8.314 J/mol·K, F is Faraday's constant, 9.649×10^4 °C/mol, T is temperature, and P_{O_2} is partial pressure of oxygen [3,4,5].

$$V = E = \frac{RT}{4F}\ln\left[\frac{P_{O_2}^{(cathode)}}{P_{O_2}^{(anode)}}\right]$$

Equation 1

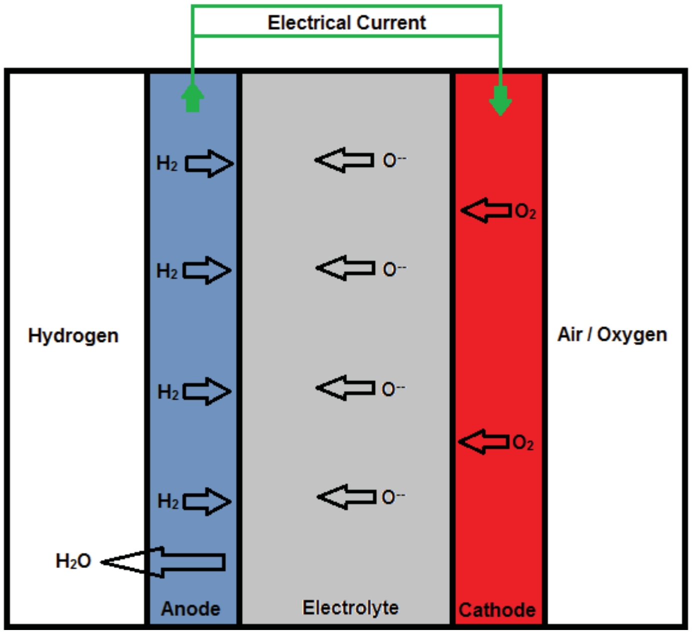

Figure 1: A basic diagram of SOFC function is shown [6].

1.2.1 Mechanisms of Ionic Conduction in YSZ

The ionic conductivity of oxygen is facilitated by the presence of mobile oxygen vacancies, V_O^{**}, in the lattice. Oxygen vacancies are created intrinsically via thermal excitation and extrinsically via charge compensation due to the displacement of the cation with dopant atoms of differing valence. The extrinsic doping effect in YSZ, is represented in Equation 2 [7,8,9,10,11].

$$Y_2O_3 \rightarrow 2Y_{Zr}' + V_O^{\cdot\cdot} + 3O_O^x$$

Equation 2

Doping is the source of the 99.999%+ of V_O^{**}, though thermal excitation is still necessary to overcome the energy barrier for vacancy motion. As temperature increases, intrinsic vacancy concentration increases, but this still has negligible contribution to ionic conductivity. It is the increased mobility of vacancies at higher temperatures that is the driving mechanism of increased ionic conductivity [2]. This necessitates operating temperatures >600 °C, but YSZ electrolyte based SOFCs commonly operate from 800-1000 °C due to the large thickness of the electrolyte relative to the mean free path of an oxygen ion [12,13]. The raised operating temperature increases vacancy concentration as well as the rate at which individual vacancy jumps occur, thus compensating for thick electrolytes, which have commonly been around 40 µm. Much effort in recent research has been in different fabrication methods to inexpensively and reliably produce <10 µm that allow for increased power density at lower operating temperatures [4,14,15,16,17,18].

In choosing dopant elements, the ionic radius is an important consideration, after the valence necessary for vacancy creation. With trivalent elements of larger radius than zirconium, 8-fold coordination of dopants is found [19]. This means vacancies tend to coordinate with the zirconium. However, with trivalent elements of smaller radius than zirconium, 6-fold coordination of dopants is found, leading to competition between dopant and zirconium over vacancies. Additionally, the coordination of oxygen vacancies affects the phase stability, with 7-fold coordination of Zr-O representing stabilized cubic zirconia [13,19,20,12].

This phase stabilizing effect of larger radius trivalent elements shifting Zr-O coordination leads towards stability of the tetragonal and cubic phases under lower dopant concentrations than with smaller radius elements, as at these lower concentrations, higher proportions of the vacancies are coordinated with the zirconium atoms relative to bulk vacancy concentration due to extrinsic charge compensation. However, the highest energy barrier of the oxygen diffusion path is around the dopant and this energy barrier increases with ionic radius. These effects suggest that the ideal dopant is one with a radius equal to zirconium, and failing that, one that is minimally larger [19]. Scandium, with an ionic radius of 88.5 pm to zirconium's 86 pm is the closest match and has been experimentally found to produce the highest ionic conductivities of stabilized zirconia. However, yttrium, with an ionic radius of 104 pm, is the industry standard with a much more firmly established research base, lower costs, and better known long term stability. Therefore, the majority of this research focuses on yttria stabilized zirconia.

1.3 Very Low Pressure Plasma Spray (VLPPS)

Plasma spray coating techniques are a very promising way to prepare electrolytes on complex surfaces. However, conventional plasma-deposited coatings have high porosities and cannot be applied in thin layers (<50 μm) suitable for electrolytes. With very low pressure plasma spray, the plasma is formed in a chamber held at pressures from 100 to 600 Pa (0.75 to 4.50 Torr) [15]. Over this pressure range, the plasma jet expands to more than 20 cm in diameter and 1 m in length. In a study by Dorier et al. [21], it was shown that plasma jet velocity and temperature increase with decreasing pressure, while plasma jet density decreases. In Table 1 below, a summary of these relationships can be seen.

Table 1: Measurements are shown from a study by Dorier et al. [21] 800 mm down the axis from the nozzle of a Sulzer Metco 03CP spray gun operated at 1500 A and 43 V, with plasma formed of H2/Ar at 3/100 SLPM.

Pressure (Pa)	Plasma Velocity (m/s)	Plasma Temperature (K)	Plasma Density (kg/m^3)
200	3200	12500	0.75 x 10^{-4}
600	2500	11000	2.5 x 10^{-4}
1000	1000	7500	6.5 x 10^{-4}

Additionally, Dorier et al.[21] showed that, at 200 Pa, the velocity and temperature are virtually constant at radial distances up to 20 mm from the jet centerline. This was attributed to laminar flow of the plasma caused by limited interaction with the diffuse chamber atmosphere. In this environment, the mean free path of atoms in the plasma increases, leading to the likelihood that radiation increases in significance for heat transfer as the collision rate drops [15,21-26].

1.3.1 Role of Plasma Forming Gases

Argon is the primary plasma forming gas and serves to carry the momentum of the plasma due to its high atomic mass. Hydrogen, being of lightest atomic mass, serves to increase the plasma enthalpy, via both its ionization energy relative to mass and the fact that it kinetically interacts with surrounding particles at a high rate at any given temperature. Helium acts similarly to hydrogen, adding less enthalpy to the plasma, but lending greater stability to the plasma arc and thus increasing deposition reliability.

1.4 Suspension Plasma Spray (SPS)

Suspension plasma spray involves the use of a liquid medium and dispersants to suspend a powder feedstock that can then be injected into the plasma stream. By using suspensions, the minimum particle size is not limited by van der Waals interactions, as with dry powder feedstock. Suspensions also allow the addition of metal salts that decompose in the plasma and are incorporated into the feedstock, enabling composition control [27]. Ethanol is the most common solvent due to its relatively low heat of vaporization, drawing 2.5 times less energy from the plasma than water based suspensions and resulting in almost a doubling of deposition efficiency [28,29]. A continuous laminar injection of suspension into the plasma core has been found to be the most effective method of injection [30,31,32]. This produces a high velocity stream, with minimal variance, as the suspension penetrates into the plasma core and results in increased entrainment in the plasma [28,33].

The high velocity of the plasma relative to the surface tension of ethanol causes the injected suspension to fragment towards an r_{min} approaching 5 μm [34,35]. Fauchais et al [37] also calculated the vaporization time of injected droplets and found that vaporization predominantly occurs after fragmentation, with 2 orders of magnitude difference between the fragmentation and vaporization times. The much higher specific surface area of fragmented droplets then allows for rapid vaporization and ionization of solvent molecules. When this is carried out in very low pressure plasma spray, the vaporization and ionization of injected ethanol was observed to take place within approximately 30 cm, or $<{}^{1}/_{3}$ of the overall length of the plasma generated during the reported research. Thus, it is over the course of the remaining plasma stream that the individual particles must melt before deposition.

1.5 Electrophoretic Deposition

Electrophoretic deposition (EPD) techniques are also able to prepare dense, thin electrolytes on complex surfaces, while doing so at significant cost savings over plasma-deposited coatings. However, fine compositional control is more challenging with EPD. EPD uses an applied voltage between an anode and cathode in a suspension to drive the particles within to flow with respect to the electric field [38]. As particles approach the electrode of opposite charge to their surface charge, the local stability of the suspension changes, allowing for deposition [39]. The key consideration to understanding deposition is the double boundary layer surrounding the particles in suspension and how it changes due to varying electric field strength, surfactants, and local ionic concentration. A general diagram of this process can be seen in Figure 2.

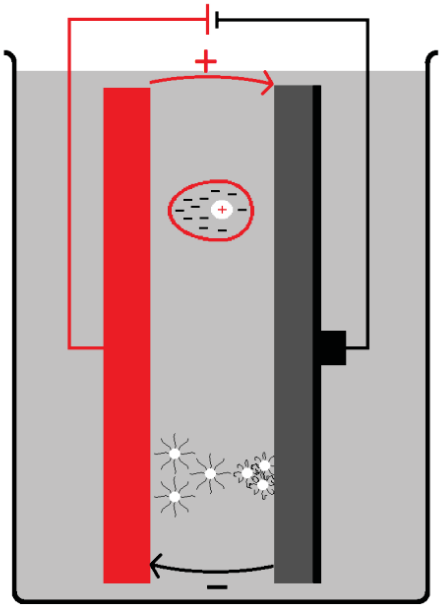

Figure 2: A diagram of anodic EPD is shown. Above shows the electrostatic mechanism of particle motion, while below shows the electrolytic coagulation deposition mechanism.

The most common description of electrophoretic deposition in literature is derived from research by Hamaker [40]. While there are multiple iterations of the factors involved, as well as fits to different electrode geometries, the core principle of Hamaker's law is that deposit yield mass is associated with the product of electrophoretic mobility μ(m^2/V·s), the local field strength E (V/m), electrode surface area S(m^2), and the particle mass concentration in suspension c_s (kg/m^3), integrated over time, as in Equation 3. The product of $\mu E s c_s$ describes the deposition rate in kg/s and thus a large assumption in this derivation is that the deposition rate is linear with respect to time. However, local field strength is affected by the growing deposit and electrophoresis causes a concentration gradient in suspension concentration near the electrodes, with an associated initiation period. Much research has addressed how best to fit Hamaker's concept to these constraints in varying systems [40,41,42,43,44].

$$Y = \int_{t1}^{t2} \mu E S c_s dt$$

Equation 3

1.5.1 Transport and Deposition Mechanisms

The study of electrophoretic particle transport and deposition has primarily focused on differentiating between the roles of electrostatic double boundary layer repulsion, steric stabilization, and the effect of electrolysis at electrodes. Ideally, particles in a stable suspension migrate to an oppositely charged electrode, their boundary layer collapses upon approach to the electrode, and an adherent densely packed deposit is formed. The interaction of the electrical boundary layer with the applied electric field is the driving force for particle transport, but the mechanism and degree of the boundary layer collapse upon approach to the electrode is still under debate [45,46,47,48,49,50,51,52].

A distinct difference of EPD from other suspension processing methods, such as slip casting, is that the transport of particles in EPD is independent of the motion of the relatively stationary liquid carrier. Instead, the particle mobility is defined with a modification to the Navier-Stokes equation to include an electrical body force term, where μ is mobility ($m^2/V \cdot s$), ϵ is permittivity ($C/V \cdot m$), ζ is the zeta potential (volts), κ is the inverse of the Debye length, η is viscosity ($Pa \cdot s$), and $f(\kappa r_p)$

is the Henry coefficient, which is dependent on the double layer thickness relative to the particle radius [53].

$$\mu = \frac{2\varepsilon\zeta \mathrm{f}(\kappa r_p)}{3\eta}$$

Equation 4

The definition of particle mobility laid out in Equation 4 is consistent with particle transport through the bulk suspension, but breaks down near the electrodes due to the effects of electrolysis and gradients in the local electric field strength [52]. Electrolysis at the electrodes changes the local ionic concentration, affecting the boundary layer composition and volume, while the shape of the diffuse secondary boundary layer is distorted away from the electrode, due to the electric field. This effect is represented in Figure 3, below.

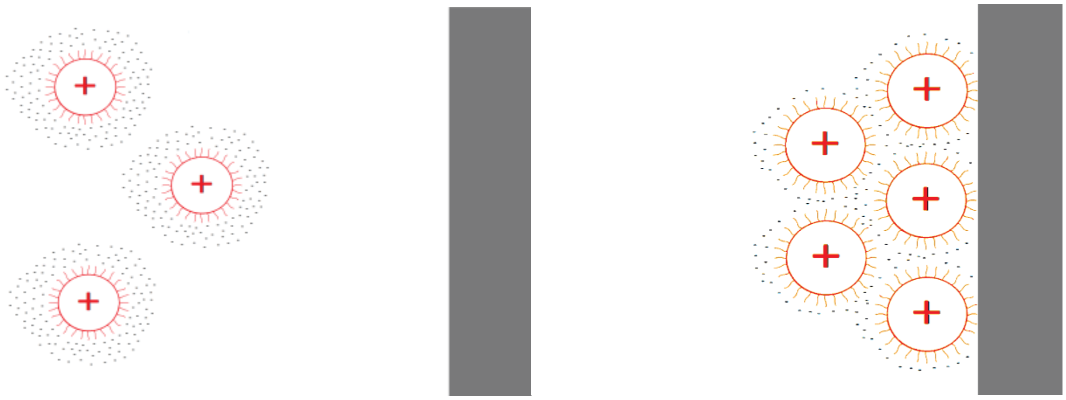

Figure 3: A diagram of an idealized anodic EPD is presented, showing the collapse of the boundary layer on approach to the deposition electrode.

The diffuse secondary boundary layer is composed of ions of the same charge as the depositing electrode, and the local concentration of these ions is expected to be lower near the electrode. This effect was modeled by De et al. [46]

and experimentally supported by Besra et al. [47] using measurement of pH vs. distance from electrode during the electrolysis of water. It was found that over the course of roughly 30s the pH would reach a steady state in which the cathode would become more basic, and the anode more acidic. In aqueous suspensions relying solely on electrostatic stabilization, this effect can be the most significant mechanism for deposition. When the pH shifts close to the isoelectric point of the particles in suspension, the localized stability loss leads to flocculation and thus deposition at the depositing electrode. It was found that the greatest deposit yields occurred when the pH shift was closest to the isoelectric point. However, if the shift to the isoelectric point occurs too far from the electrode, premature flocculation can occur [47].

As flocculation occurs farther away from the point of deposition, irregular coatings with greater porosity are created, until premature coagulation leads to Stoke's Law settling and loss of coating development. Well controlled deposition of high packing density coatings relies on maintaining high inter-particle repulsion upon approach to the electrode. However, contact with the electrode will discharge a depositing particle, causing subsequent depositing particles to be attracted to the deposit in similar fashion to the bare electrode. This effect can be partially offset by the resistance of the deposit, but generally leads to lower packing density. Note that deposit resistance is usually greater than that of the bulk suspension, though it is dependent on differences between particle, dispersant, and solvent conductivities, as well as packing density and Debye length relative to the diameter of deposited particles. As deposition rate and electric current are proportional, the deposition rate is greater at regions of lower resistance, with the thinnest deposit. This suggests that lower conductivity deposits will be more likely to form uniformly, in terms of thickness, though maximum deposit thickness is limited by the deposit conductivity.

Steric stabilization can compensate for the effect of electrolysis at the electrodes, since the polymer chains are directly adsorbed onto the particle surface, providing inter-particle repulsion as the diffuse boundary layer collapses. Also, the polymer can function as a binder upon drying to increase green body strength of the deposit and reduce capillary stresses. Finally, since the diffuse boundary layer is formed around charge interaction with the polymer, the electrostatic repulsion in suspensions is less affected by the specific material properties of the depositing particle, meaning the process is more reproducible among varying applications. Mizuguchi et al. [52] showed this using nitrocellulose as a steric stabilizer in the deposition of Al_20_3, TiO_2, SiO_2, and W, among many other systems.

1.5.2 Effects of Suspension and Operating Parameters

As deposition proceeds, the relative concentrations of all the suspension components change. This problem can be solved by continually cycling fresh suspension into the process, but efficacy would be greatly improved by instead adding a concentrated suspension of compensatory constituents to those lost during deposition. However, this first requires quantification of how the suspension concentration changes during deposition. Nevertheless, the general trend and difference between deposition methods can be seen in Figure 4, below, showing

deposition under: 1.) constant current & suspension, 2.) constant current & depleting suspension, 3.) constant voltage & suspension, and 4.) constant voltage & depleting suspension.

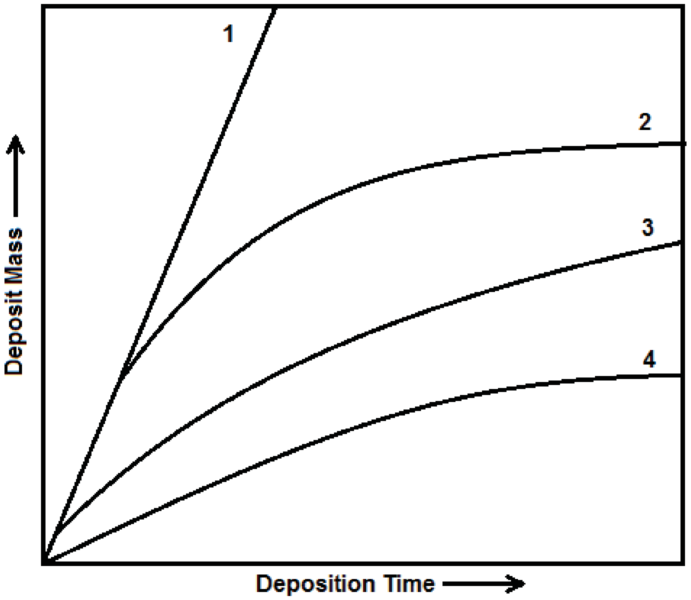

Figure 4: A diagram is shown of EPD yield vs. time under conditions of: 1.) constant current & suspension, 2.) constant current & depleting suspension, 3.) constant voltage & suspension, and 4.) constant voltage & depleting suspension [47].

The properties of the electrode itself can play an important role in EPD. A non-reactive and highly conductive electrode is generally ideal, but in applying EPD to SOFC production, low conductivity substrates must be used, such as NiO-YSZ. Research by Besra et al.[54] used suspension infiltration of NiO-YSZ substrates with open porosity to raise the conductivity (Figure 5). They found uniformity and deposit yield to have a positive correlation to substrate porosity.

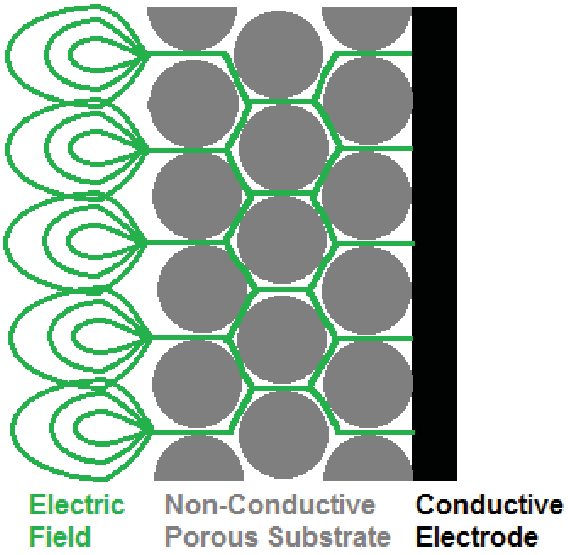

Figure 5: A diagram is shown representing a mechanism by which a conductive path through a porous substrate can allow EPD, as exemplified in research by Besra et al.[54]

Another method to deposit on low conductivity substrates is to apply a thin conducting layer to the low conductivity substrate's surface. Hosomi et al.[55] used this technique with graphite as the conductive layer, but found the subsequently produced SOFC underperformed those produced via the infiltration technique. It was believed the resultant deposit contact was less adherent and caused an increase in cell contact resistance.

1.6 Overview of the Present Study

The focus of the research presented in this thesis was on deposition of compositionally modified and functionally graded solid oxide fuel cell electrolytes via the suspension based processing methods of very low pressure plasma spray and electrophoretic deposition. The role of suspension constituents in deposition was characterized through a parametric study. Suspensions, substrates, and electrophoretically deposited coatings were prepared at Purdue University; very low pressure plasma spray electrolyte coatings were applied at Sandia National Laboratories' (SNL) Thermal Spray Research Laboratory (TSRL). The resultant electrolytes were characterized based on microstructure, composition, and phase assembly, as well as their performance as part of a complete solid oxide fuel cell, in button cell testing of open circuit voltage, power density, and impedance spectroscopy.

CHAPTER 2. EXPERIMENTAL AND ANALYTICAL PROCEDURES

This chapter describes the experimental approach utilized to fabricate and characterize SOFCs based on very low pressure suspension plasma spray and electrophoretic deposition of YSZ and GDC electrolytes on NiO-YSZ anode substrates.

2.1 Coating Fabrication via Very Low Pressure Suspension Plasma Spray

The first four generations of electrolyte coatings were created at Sandia National Laboratories' Thermal Spray Research Laboratory, using their very low pressure plasma spray system consisting of a ~3500 L stainless steel water cooled vacuum chamber, a Sulzer Metco 03CA plasma torch, a 2000A, 50V Halmar power supply, and a N_2 pressurized suspension feed system, shown in Figure 6. The vacuum chamber could pump down to <100 mTorr while the torch was inactive. During deposition, the pressure would rise to 2.4 – 5 Torr depending on plasma power, suspension injection, and flow rates of argon, hydrogen, and helium into the arc chamber. See Figure 7 for the dimensions of the cathode and anode setup.

Figure 6: An image of the vacuum chamber at the SNL's TSRL is shown.

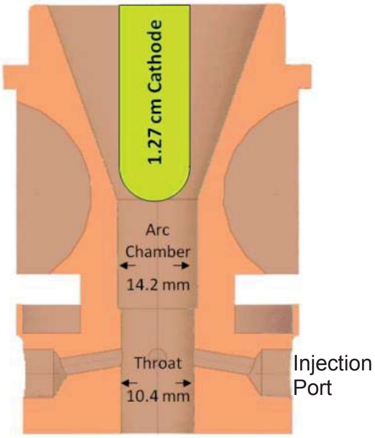

Figure 7: A diagram of the cathode and anode plasma gun setup used at the TSRL is shown.

All suspensions were injected orthogonally into the torch throat through a 230 μm diameter ruby straight hole nozzle, with a back pressure of ~3900 Torr, resulting in an injection velocity of ~20 m/s and a flow rate of ~43 g/min. The flow rate and injection velocity were calculated based on logging of mass change during deposition and the nozzle diameter. A second feed supply of ethanol was also used to keep the injection nozzle cool before suspension injection, as well as to clean the feed system after deposition, as clogging would otherwise occur frequently. Standoff distance was varied from 89-125 cm, with one substrate fixture designed to simultaneously test deposition within a 15 cm range.

Three types of substrate fixtures were used over the course of plasma spray research. The original design sought to characterize the stand-off distance sensitivity, which was found to be minimal within the 15 cm tested range from 109-124 cm. Subsequent design generations sought to address the thermal shock issues associated with very low pressure plasma spray, in which an air knife cooling method raises the chamber pressure, interferes with the deposition, and convective cooling efficacy is significantly reduced. The first substrate fixture was a stair step design allowing for simultaneous testing of three different stand-off distances, spaced 7.5 cm apart, as seen in Figure 8. This design was found to heat up rapidly during spraying, in excess of 1200 °C, while the torch passed over it. It would then cool quickly enough, when the torch moved away, to cause thev substrates to fracture due to thermal shock. This required a reduction of plasma enthalpy in initial experiments via limiting gas helium composition and torch power.

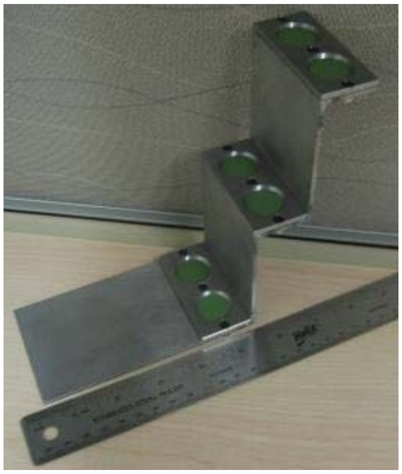

Figure 8: An image of the stair step sample fixture, with substrates loaded is shown.

The second substrate fixture was a water cooled copper plate, as seen in Figure 9, below. This fixture, which had a thermocouple inserted under the substrates, managed to reduce the maximum temperature of the substrates to <800 °C, enabling a wider range of plasma enthalpies to be tested, though it was insufficient to entirely resolve the substrate cracking issue in the highest enthalpy range of the torch as it still facilitated rapid temperature change of the substrate. The final and ultimately most successful sample fixture consisted of a stainless steel cylinder heat sink of 12.7 cm diameter and 15 cm length, implanted with a thermocouple, and used to maintain heating and cooling rates <20 °C/minute. Unfortunately, the hydrogen feed system at the TSRL failed shortly after this solution was proven and thus the highest enthalpy plasmas were never able to be utilized for electrolyte deposition research. This plasma enthalpy limitation, when combined with the enthalpy reduction caused by vaporizing ethanol from the suspension, was found to lead to insufficient melting of particles in the plasma.

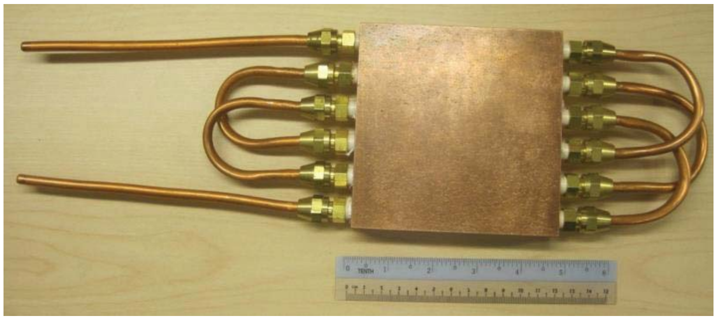

Figure 9: An image of the cold plate sample fixture is shown. This sample fixture allowed for a reduction in substrate temperature and an increase in temperature stability over the course of a spray run.

2.2 Coating Creation via Electrophoretic Deposition

Electrophoretic deposition allowed for the same or similar suspension feedstock to be used for SOFC electrolyte fabrication, including the continued progression of nitrate-doped suspension research, while eliminating the travel and reliability issues faced with applying coatings with very low pressure plasma spray. Thus, these can serve as good comparison processes, elucidating the effects of the differing thermal histories, with fixtures designed to maximize the potential similarities between the two. The primary function of the electrophoretic deposition fixture was to facilitate use of the NiO/YSZ substrates as the anode, described previously in Figure 3, while a stainless steel plate served as the cathode. The fixture allowed unstressed attachment of the substrate via solvent free silicone sealant to a small enclosed chamber, submerged in the suspension, in which a graphite electrode connected the substrate to the negative power supply lead. The graphite electrode consisted of a graphite sheet, adhered with graphite paste, which is necessary to uniformly distribute the applied voltage, as the resistivity of the substrate caused electric field strength to vary enough to induce patterned deposition otherwise. Images and diagrams of the EPD fixture can be seen in Figure 10.

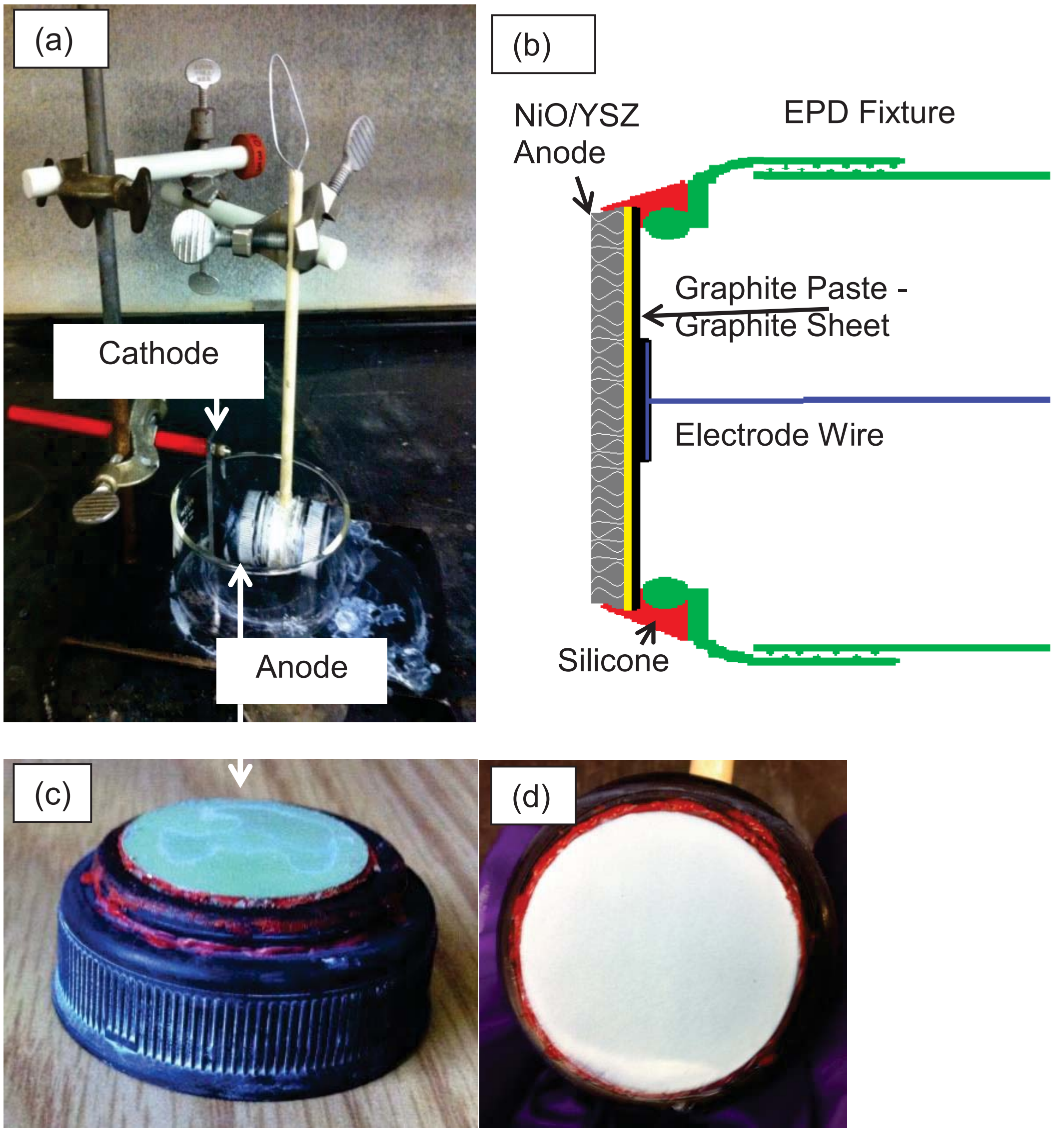

Figure 10: Images of the EPD fixture are shown. (a) shows the complete fixture, with NiO-YSZ substrate as the anode, (b.) shows a schematic view of the anode fixture from (a), (c.) shows an anode (in the oxidized higher resistance state), and (d.) shows a YSZ electrolyte deposit formed after EPD.

The distance between cathode and anode was held constant at 10 mm, with a rubber ring cut to this dimension serving as the benchmark and ensuring consistent parallel separation between electrodes. A Spellman SL150 power supply was used, with selectable constant current or constant voltage deposition. The majority of depositions used a constant current, as that has been found to produce a more linear relationship of deposit yield versus time than constant voltage deposition, as described in chapter 1. For any given test, the response current or voltage was logged with an Agilent 34401A Digital Multimeter. Each deposition began with a 5 minute presoak of the EPD fixture in the suspension to ensure the open porosity of the anode substrate was fully infiltrated with suspension. After deposition, the fixture was removed from the suspension and the fixture cap containing the anode was removed and placed in an enclosed chamber resting above a pool of ethanol. This slowed the otherwise rapid ethanol evaporation, reducing capillary stresses, and also protected the deposit.

2.3 Suspension Preparation

Suspensions were prepared by dispersing a powder in ethanol and adding either polyethylinamine (PEI) or Triton QS-44 phosphate ester as a dispersant. Optionally, polyvinyl butyral (PVB) and or acetic acid were also added as a binder or electrophoresis modifier, respectively [50,56,57]. Scandium nitrate was also added in some suspensions to modify the composition of the finished coating, via either incorporation during plasma spraying or diffusion during post deposition sintering for EPD. The dispersed powders included: yttria-stabilized zirconia

(YSZ), gadolinia-doped ceria (GDC), and erbium-stabilized bismuth (ESB). The YSZ included a variety of particle size and specific surface area powders, including two 8 mole % YSZ powders and one 10 mole % YSZ powder. The two 8 mole % YSZ powders comprised a 40 m^2/g powder from Inframat Advanced Materials and a 13 m^2/g powder from Tosoh. The 10 mole % YSZ powder had a specific surface area of 6 m^2/g. The GDC powder was 10 mole % gadolinia, from NexTech Materials, with a specific surface area of 12 m^2/g. The particle size distributions of the YSZ powders can be seen in Figure 11 & Figure 12, below, as measured with a LS230 Coulter Counter. Note that the particle size distribution was measured in a medium of water, which likely led to less dispersion of particles and resulted in the bimodal distribution shown.

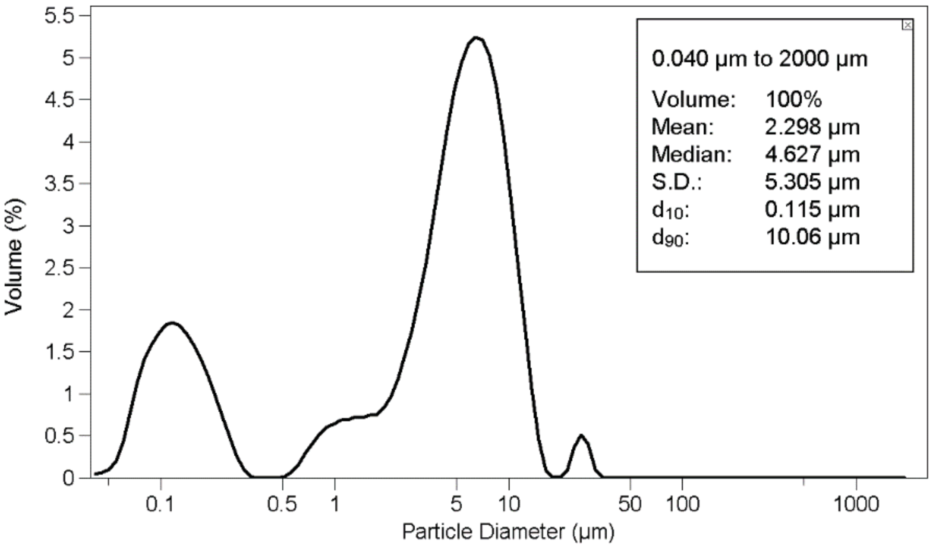

Figure 11: Coulter Counter measurement of particle size distribution are shown for 40 m^2/g 8 mole % YSZ from Inframat Advanced Materials.

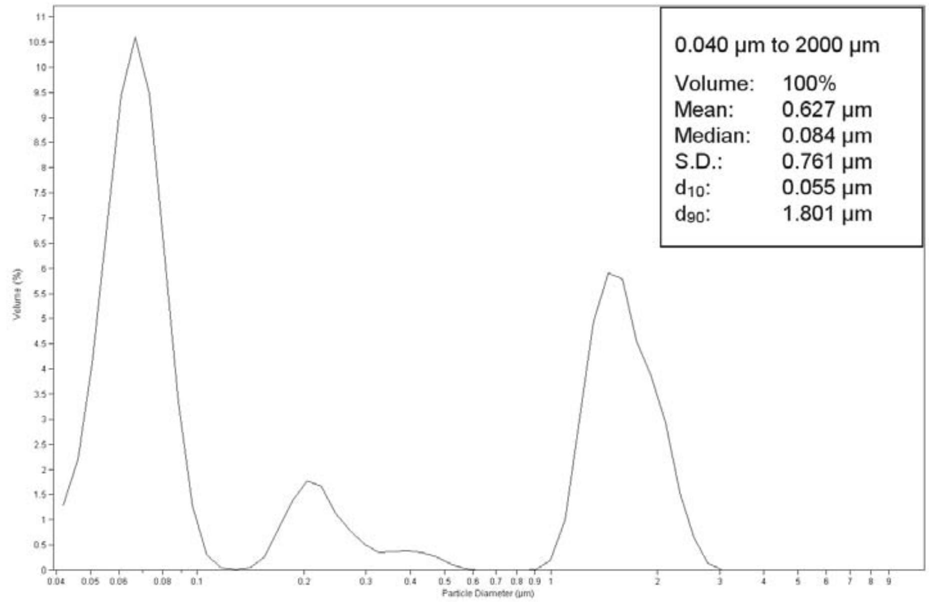

Figure 12: Coulter Counter measurement of particle size distribution are shown for 13 m^2/g 8 mole % YSZ from Tosoh

The dispersants were either the phosphate ester Triton QS-44 or a low M_n (~1200) polyetheleneimine (PEI), both from Sigma Aldrich. Two different dispersants were necessary as the Triton QS-44 went out of production a year into research, although the use of PEI resulted in improved suspension stability over Triton QS-44. Both dispersants were found to have optimal effectiveness at a weight fraction of 0.01 to the total suspension. The amounts of each component were calculated based on Equation 5 and Equation 6, where V is volume (mL), ρ is density (g/mL), and w is weight fraction, with subscripts T, e, d, y, representing total, ethanol, dispersant, and powder, respectively.

$$V_T = V_e + V_d + V_y$$

Equation 5

$$\frac{\rho_d V_d}{\rho_e V_e + \rho_d V_d + \rho_y V_y} = w_d$$

Equation 6

In select suspensions, acetic acid was added based on the ethanol content of suspensions up to 10^{-1} M, with a range within 10^{-2} M found to have the greatest utility for affecting deposition, as discussed in chapter 4. Also, $Sc(NO_3)$-XH_2O, with a m_w of 287.1 g/mol, an amount that can vary slightly by supplier due to varying water content, was used as a doping agent in some suspensions, up to 16 mole % scandium. Dopant additions were calculated based solely on achieving the desired composition, with mole fraction numbers representing the scenario of complete diffusion into the YSZ feedstock, as they were soluble in ethanol and did not play a role in powder dispersion. As such, the actual volume fraction of feedstock in doped suspensions was marginally lower than baseline suspensions. This small deviation was viewed as acceptable as it allowed for batch production aimed at minimizing variation between suspensions. Note also that for every 1 mole % scandium successfully incorporated into the YSZ, this represents only 0.5 mole % scandia incorporation.

The final step of preparation was ball milling the suspensions for 3 hours in 500 mL baffled bottles. The suspensions were combined with 10 mm YSZ cylindrical milling media and milled at ~140 rpm. An overview of suspension preparation can be seen in Figure 13. The zeta potential, ζ, and electrophoretic mobility, μ, of suspensions used in EPD were measured with a Malvern Zatasizer Nano S. Also, thermogravimetric analysis (TGA) of suspension and coating constituents was performed using a TA Instruments Q50 TGA.

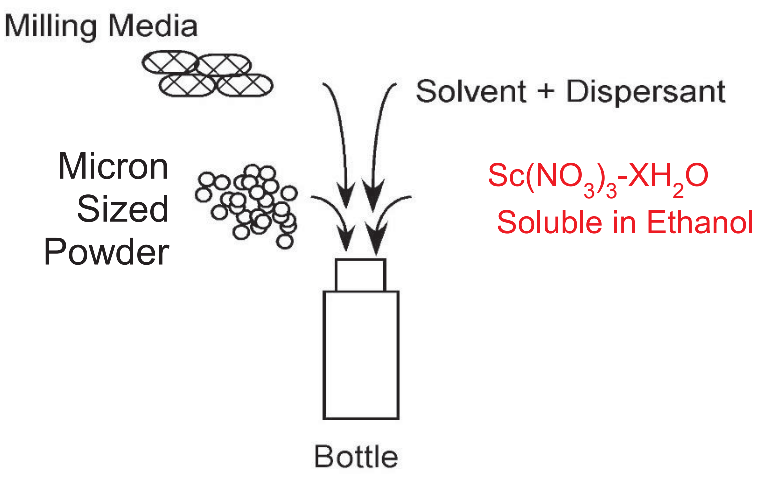

Figure 13: An overview of suspension preparation is shown.

2.4 Substrate Preparation

Substrates were designed to serve as the anode component of both a SOFC and an EPD electrode. They were constructed out of laminated sheets of tape cast 50/50 NiO-YSZ, purchased from ESL Electroscience, with each layer 180 μm thick [58,59,60,61]. Substrates were constructed with 1, 3, 6, and 10 layers, with the majority of research focused on the 10 layer substrates due to their superior mechanical strength and resistance to curvature during co-sintering with deposited electrolyte coatings. The sheets were laminated with a warm press and die, operated at 70 °C and 21 MPa, for 20 minutes. For EPD, the resultant discs were bisqued and reduced at 1000 °C for 2 hours in an Ar/5%H_2 atmosphere, but were then co-sintered after EPD at 1400 °C for 2 hours. For plasma spray deposition, the discs were instead sintered at 1400 °C for 2 hours before deposition, as this improved substrate mechanical strength and plasma sprayed coatings deposit at high densities that do not require co-sintering with the substrate. The progression from tape casting to anode substrate can be seen in Figure 14.

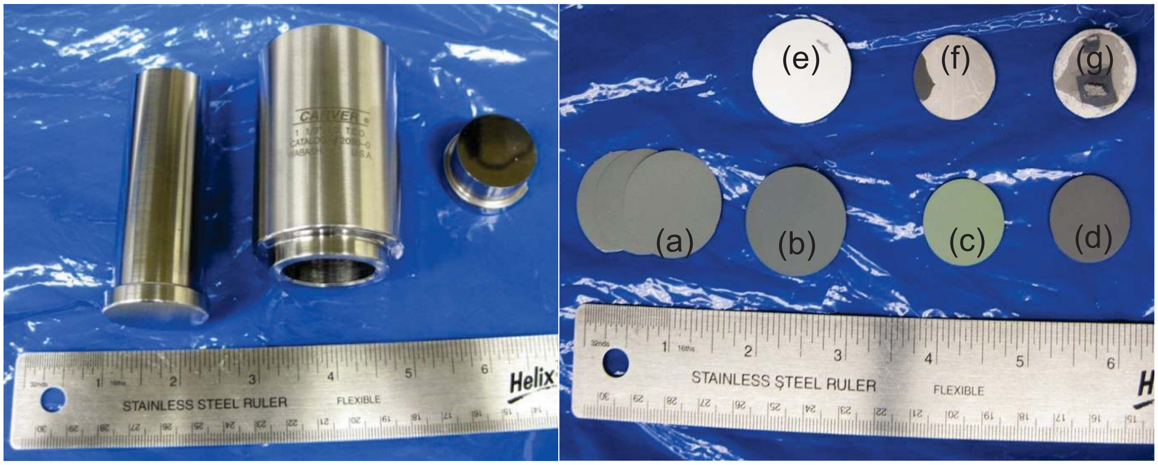

Figure 14: Images of the die (left) used to laminate the anode layers as seen on the right image showing the progression: (a) unlaminated sheets of NiO-YSZ, (b) warm-pressed laminated sheets of NiO-YSZ, (c) sintered laminated sheets of NiO-YSZ (in oxidized state), (d) sintered laminated sheets of NiO-YSZ (in reduced state), (e) an example of the initial material system used: NiO-YSZ with a YSZ electrolyte laminated sheet on top, (f) a sintered version of (e), in which the electrolyte delaminated, and (g) a complete fuel cell after testing, showing the cathode side (the white border is the bonding cement, the dark grey is the LSM-YSZ cathode material with platinum electrodes bonded to it, and the pearlescent area is exposed electrolyte)

2.5 Solid Oxide Fuel Cell Performance Evaluation Methodology

The substrate preparation and deposition processes previously described supplied samples of thin electrolyte coatings on NiO-YSZ substrates, which served as the basis for the creation of anode supported button cells, tested using four probe points, two for current, and two for voltage measurement. To these samples, a cathode paste of lanthanum strontium cobalt ferrite (LSCF), from NexTech Materials, was then applied on top of the electrolyte using screen printing and a mask to produce 1 cm^2 contacts. A platinum mesh was then pressed on the wet cathode with a 100 g weight to ensure contact. After drying the cathode under a heat lamp, alumina paste, Cermabond 552-VFG, was applied to the edges of the platinum mesh and the remaining untested surface. This alumina paste served as a sealant, as well as to secure the electrode from pulling off during the remaining preparation and testing phases. After the alumina paste had dried, the 100 g weight was removed and each cell contact area was measured with calipers. Then the cells were heat treated at 1100 ºC for 2 hours in air to cure the LSCF. This was followed by a substrate reduction at 600 ºC for 2 hours in an Ar/5%H_2 atmosphere, which was found to improve consistency of electrode attachment on the anode side of the cell.

The electrode attachment on the anode side followed a different procedure from the cathode, serving also to attach the SOFC to the testing fixture. First, the anode was polished with a 400 grit SiC pad to remove any debris from the crucible, then platinum paste was screen printed in alignment with the cathode electrode. The cell was then placed on the top of the testing fixture, while the fixture was in a vertical orientation. The fixture itself is set with a platinum mesh suspended around the H_2 inlet alumina tube, which was aligned with the cell and temporarily sticking out beyond the edge of the outer alumina tube sheath that contains the H_2 atmosphere. Once solid contact between the platinum mesh and the anode is ensured, the H_2 inlet tube is withdrawn into the fixture until the cell edges contact the outer alumina tube. At this point, a 100 g weight was placed atop the cell, with a short alumina tube of the same diameter as the outer fixture tube used to distribute the force and prevent contact with the cathode. The Ceramabond alumina paste was then used to seal the SOFCs to the outer alumina tube. After drying, the weight was removed and the final wire connections to the cathode side platinum mesh were made. The layout of fuel cells during testing can be seen in the diagrams in Figure 15.

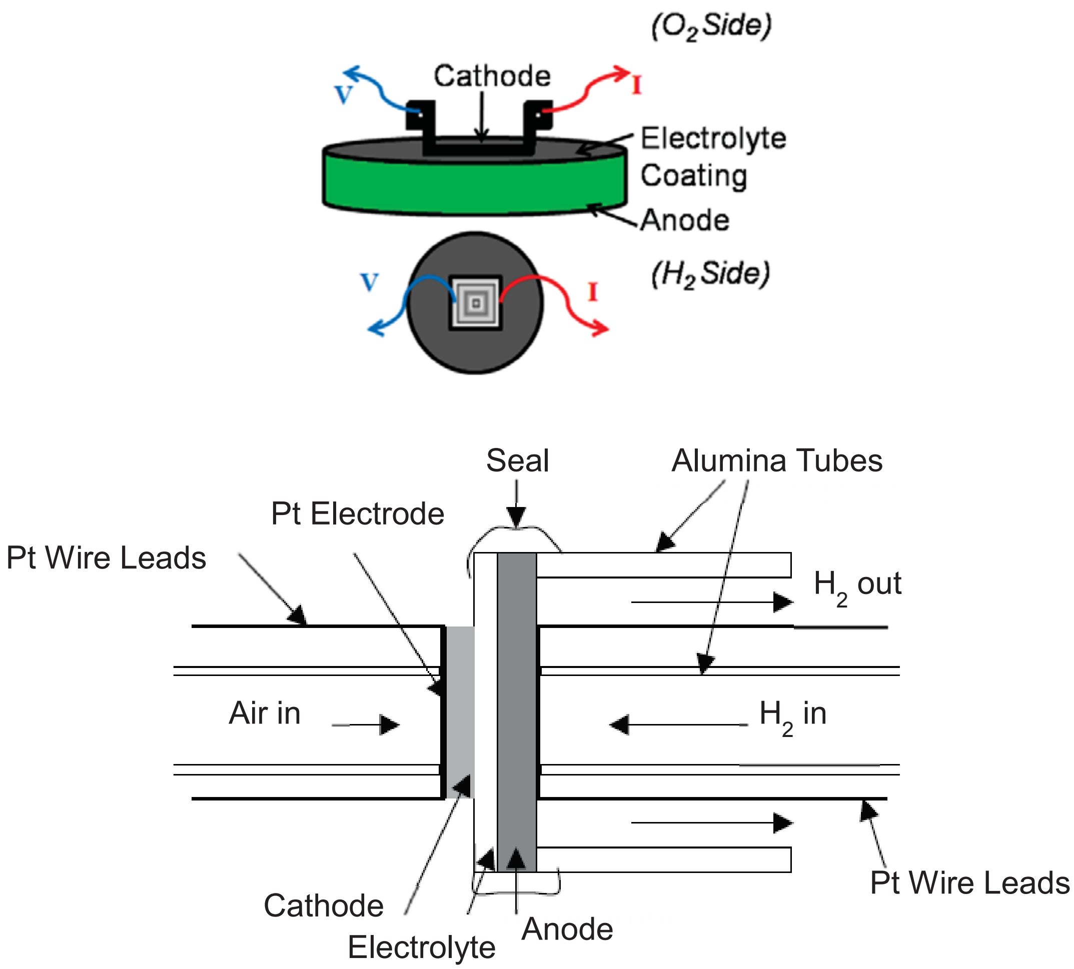

Figure 15: A diagram is shown of a complete SOFC with electrodes attached using a four point method. Views of the side and bottom of the cell itself can be seen above, while the cell's layout within the testing rig can be seen schematically below.

The fuel cell testing fixture was then placed in a tube furnace, in a horizontal orientation, and electrodes were connected to the Solartron equipment, with active recording of open circuit voltage beginning at this time. Then, the air supply tube was placed against the platinum mesh on the cathode, a thermocouple was inserted in contact with the alumina seal adjacent to the cathode, and H_2 was hooked up at a minimum flow of 15 ml/min, through a water bubbler at approximately 25 ºC, and exhausted through an oil bubbler into a fume hood intake. The furnace was programmed to cure the alumina paste and then hold at testing temperatures from 600 – 900 ºC. The heating profile was 3 ºC/min to 100 ºC, hold 3 hours, then 3 ºC/min to 260 ºC, hold 3 hours, then 5 ºC/min to 600, 700, 800, & 900 ºC, with 30 minute holds at each temperature. Actual testing used manual temperature holds in addition to the allotted 30 minutes. When 600 ºC was reached, H_2 flow was increased to 150 ml/min and the cell was allowed to equilibrate before further testing, based on stabilization of open circuit voltage. After testing at 900 ºC, the cell was held for 24 hours, with ongoing potentiostatic testing at the voltage measured for peak power to establish performance stability and any current conditioning effects. The cells were then retested on holds during the cooling cycle. An image of the testing rig can be seen in Figure 16.

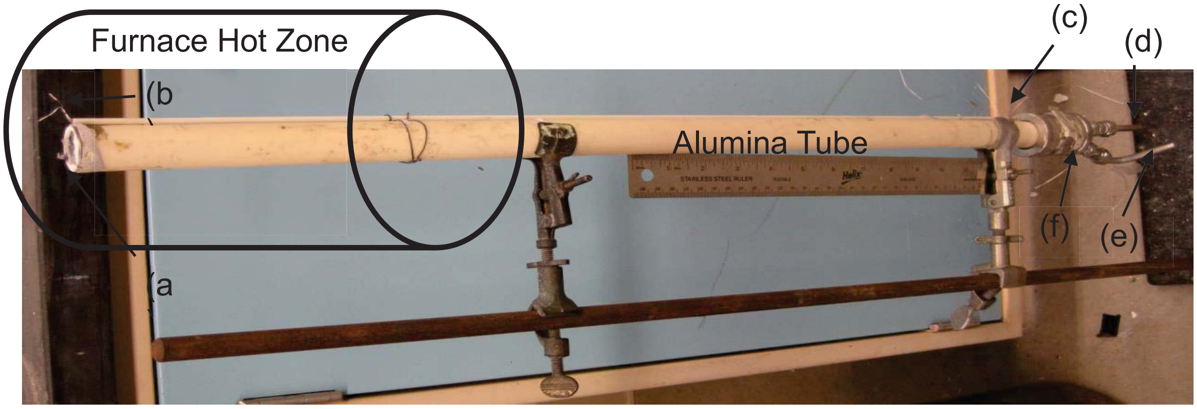

Figure 16: An image of the fuel cell testing rig outside of the furnace and fume hood, showing: (a) the cathode-side of the SOFC, (b) the cathode-side platinum electrode wires that attach to the fuel cell, (c) the cathode-side platinum wire measurement output connections, (d) the H2 gas input tube, (e) the exhaust gas tube (which feeds through an oil bubbler and out a fume hood), and (f) the anode-side platinum wire measurement output connections.

At each given testing temperature, the open circuit voltage was measured and allowed to equilibrate for 10 minutes, then electrochemical impedance spectroscopy (EIS) was performed at open circuit voltage. EIS uses a linear electrical perturbation, in this case a frequency sweep from 0.1 – 100 kHz of an AC signal with an amplitude of 10 mV, and measures the response signal [62,63,64]. Although the impedance measurement and corresponding electrical processes are represented in the time domain, electrical circuit theory has developed simplified equations based on transformation to the frequency domain [65,66]. The criterion for validity of this transformation was based on linear systems theory, which requires the system have linearity, with finite numbers at each frequency, stability, and causality. Linearity means that linear equations can describe the response and all response frequencies are within the finite range of the applied frequencies, which is achieved with the 10 mV sinusoidal perturbation voltage. Stability means the system is at a steady state before testing and returns to that state after testing is complete. Causality means the input signal is the cause of the output signal, the measured effect [67, 68].

The impedance measurement contains real and imaginary components, which are often represented in a Nyquist diagram as [Real(Z] versus – [Imaginary(Z)]. Resistive processes are observed in the real domain, while capacitive processes are observed in the imaginary domain. A typical Nyquist diagram takes the form of one or more semi-circles, depending on the number of contributing components to the impedance and polarizable interface surfaces between them. This impedance spectra can be evaluated by fitting the data to an equivalent circuit that represents the physical and electrochemical processes occurring in the cell, such as oxygen dissociation, charge transfer resistance, bulk ionic conduction in the electrolyte, and grain boundary ionic conduction in the electrolyte. An example equivalent circuit from a cell with a LSCF cathode, YSZ electrolyte, and NiO/YSZ anode is shown in Figure 17, where L represents the inductance in the platinum wire probes, R_Ω the overall ohmic resistance of the electrodes, anode, electrolyte, and cathode, R_1 the high frequency arc resistance, R_2 the low frequency arc resistance, Q_1 the high frequency arc constant phase element, and Q_2 the low frequency arc constant phase element. The admittance, Y, of a given constant phase element, Q, is defined in Equation 7, where Y_0 is the amplitude, n the exponent component, and ω the angular frequency [69].

$$Y = Y_0(j\omega)^n$$

Equation 7

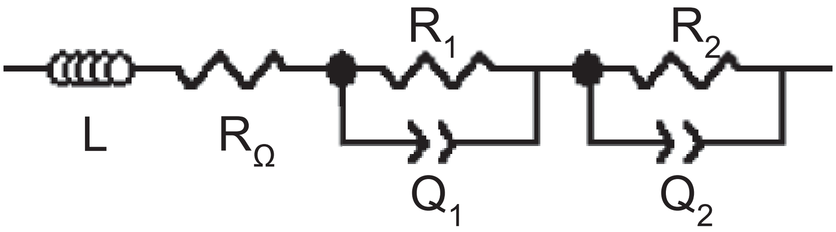

Figure 17: An equivalent circuit representing impedance tested SOFCs is shown [62].

Solartron’s Zplot software was used to calculate the fitted parameters based on the impedance spectra and a convergence algorithm with a maximum of 100 iterations and 10 optimization iterations, with initial values entered from estimation of the resistance from the impedance spectra and capacitance from literature for systems of the same materials, testing configuration, and similar microstructure

[62,67,69]. Convergence was confirmed by retesting to ensure optimized values reoccurred, with evaluation of the fit to experimental data using least sum of squares (χ^2) values below 10^{-6} to indicate a quality fit.

The potentiodynamic testing regime allowed at least 10 minutes at open circuit voltage after completion of EIS, at which point the voltage was decreased from open circuit by 10 mV/s, with the current response measured. Power density was calculated from this measurement and plotted concurrently with the IV curve, as can be seen schematically in Figure 18. The shape of the IV curve indicates some of the processes and limitations in the cell, beginning with the Y intercept at the open circuit voltage of the fuel cell, which should be near to the theoretical value calculated from Equation 1, around 1.1V.

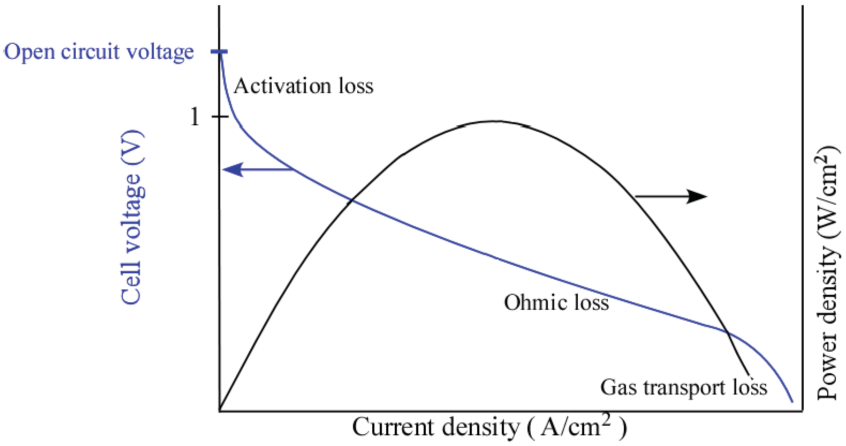

Figure 18: A schematic of potentiodynamic test results is shown, with the left Y1 axis representing voltage, the right Y2 axis representing power density, and the X axis representing current density.

At the open circuit voltage, no practical amount of current can be drawn, but as more current is drawn, there are voltage losses due to activation polarization, ohmic polarization, and concentration polarization. Activation polarization, also referred to as reaction rate losses, are most significant at low current densities and represent electronic barriers to current and ion flow. Ohmic polarization, or simply electrical resistance loss, is directly proportional to current flow. Concentration polarization, or gas transport loss, is caused by the cell reaction rate exceeding the rate at which gas diffuses into the cell or through a rate limiting component in the cell.

2.6 Microstructure and Phase Characterization

Deposit morphology was studied using a FEI Philips XL-40 scanning electron microscope (SEM), with Au/Pd sputtered films on samples to reduce charging. The field emission gun was operated at an accelerating voltage of 25 kV and working distance of 10mm for the majority of images, with divergences from this standard associated with high depth of field topographic images, which are individually noted. Scion Image software and stereological techniques were used to analyze micrographs for electrolyte thickness and density measurements. Energy dispersive X-ray spectroscopy (EDS) based composition analysis was used to confirm nitrate doping efficacy, as well as to highlight microstructural features using X-ray map images.

X-ray diffraction (XRD) was used for phase characterization, with a Siemens D8 Focus, employing a λ = 0.15406 nm Cu K_α source, at a scan rate of 2 º/min and a slit size of 0.963º. Both the oxidized and reduced state NiO-YSZ substrates were characterized, as well as the source powders for the suspensions, the as-sprayed SPS/VLPPS electrolyte coatings, and electrolytes of each process sintered at 1400 ºC for 2 hours. This was necessary to differentiate between the like materials of the substrate and electrolyte, as well as the potential processing steps in which phase changes could occur. The effect of dopants on phase composition as well as differences between VLPSPS and EPD were thus characterized.

CHAPTER 3. DESCRIPTION AND ANALYSIS OF VLPSPS COATING EXPERIMENTS

Through the experimental approach detailed in this chapter, the primary constraining parameters of very low pressure suspension plasma spray (VLPSPS) were characterized, particularly as they relate to the deposition of solid oxide electrolytes on anode supported substrates and the ability to modify the final deposit composition via metal salts dissolved within the suspension. Reliability was a significant issue faced in these experiments, associated with the side effects caused by internal suspension injection into a plasma spray nozzle combined with the heat and mass transfer mechanisms associated with operating in a low ambient pressure environment. Also, it must be noted that a separate source of experimental variability was due to the complex amalgamation of aging custom components used to create the system utilized at Sandia National Laboratories (SNL) Thermal Spray Research Laboratory (TSRL). Coatings were created during three visits in May of 2010, the summer of 2011, and March of 2012, here referred to as sample sets A, B, and C, respectively. A final visit in September 2012 also occurred, but a failure in the Hydrogen supply precluded viable coating deposition, allowing only effective study in heat transfer processes. The operating parameter of these first three visits can be seen in Table 2, Table 3, and Table 4 in section 3.2.

3.1 Influence of Injection and Plasma Interaction on Coating Formation

The ambient pressure of the plasma spray chamber is the largest controlling factor for the expansion and flow characteristics of the plasma torch, which in turn affects the energy density, feedstock residence time, and deposition profile of the torch [15]. The primary controlling parameters of the ambient chamber pressure are gun power, plasma forming gas composition, gas flow rate, feedstock injection, and chamber pumping capacity. A complication of using suspension feedstock in a very low pressure environment is the combination of plasma enthalpy loss, due to heating and vaporizing the suspension medium, with the resultant expansion of the plasma and increase in the ambient chamber pressure. This means that the heating of the suspended powder is delayed, occurring outside the hottest, most dense plasma volume, the overall plasma enthalpy is reduced, and the low chamber pressure allows the plasma to expand farther than in atmospheric suspension plasma spray, thus further reducing the plasma enthalpy. However, this effect is countered by the increased residence time of the expanded plasma plume. Due to these interactions and competing effects, it is best to control the chamber pressure to a fixed point for any given series of tests. Yet, the tradeoff of operating at a fixed chamber pressure is inevitably to operate at a higher pressure than the best possible by the equipment. Ultimately, the ability to control the chamber pressure is the ability to select different deposition profiles [15,21,34].

The operating conditions have a significant effect on the minimum achievable chamber pressure during continuous plasma spraying. Higher power, gas feed rate, and powder feed rate can raise the chamber pressure by 250 Pa. In Figure 19, Figure 20, the difference between a low power and a high power spray can be seen, without any feedstock injection. This difference alone leads to a 1 Torr pressure change. In the case of suspension plasma spray, the chamber pressure is raised by another 1 Torr due to ethanol vaporization. While the minimum steady-state chamber pressure is limited by the operating conditions, above this minimum the CAPS chamber can correct for these differences and spray at fixed pressures. In Figure 21, the plasma can be seen at operation in the vacuum plasma spray (VPS) regime at around 13 kPa.

Figure 19: This image shows the plasma at the lowest achievable steady-state pressure of the TSRL's CAPS system at low power settings. Gun amperage is at 1000 A, with 50 slpm Ar

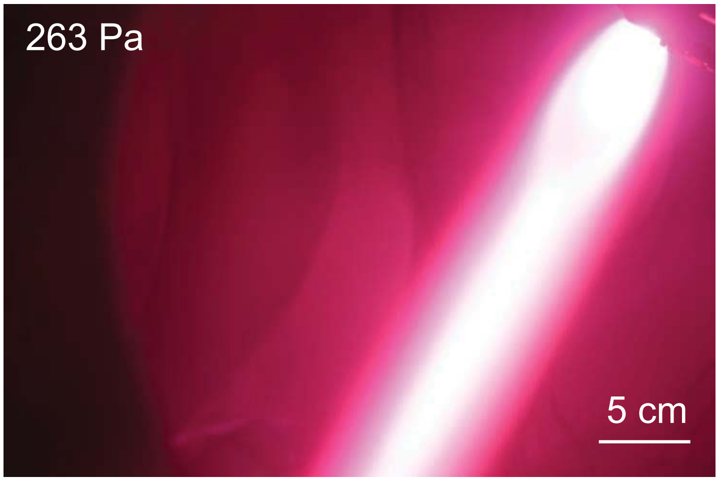

Figure 20: This image shows the plasma at the lowest achievable steady-state pressure of the TSRL's CAPS system at high power settings. Gun amperage is at 1800A, with 60 slpm Ar, 7 slpm H2, & 59 slpm He

Figure 21: This image shows the plasma at 12800 Pa steady-state pressure in the TSRL's CAPS system at high power settings. Gun amperage is at 1800A, with 60 slpm Ar, 7 slpm H2, & 59 slpm He

The CAPS chamber allows for ambient pressure control within tenths of a Torr. As chamber pressures drop to <300 Pa, even five Pa changes can have a clear visible effect on the plasma, as seen in Figure 22. The primary methods for controlling the chamber pressure are through the selection of operating vacuum pumps, a Stokes and a Kinney pump were available, six argon window blow-off valves, and a butterfly flow regulator valve on the stokes pump. Above 1300 Pa, the automated chamber pressure controls were sufficient alone to control chamber pressure.

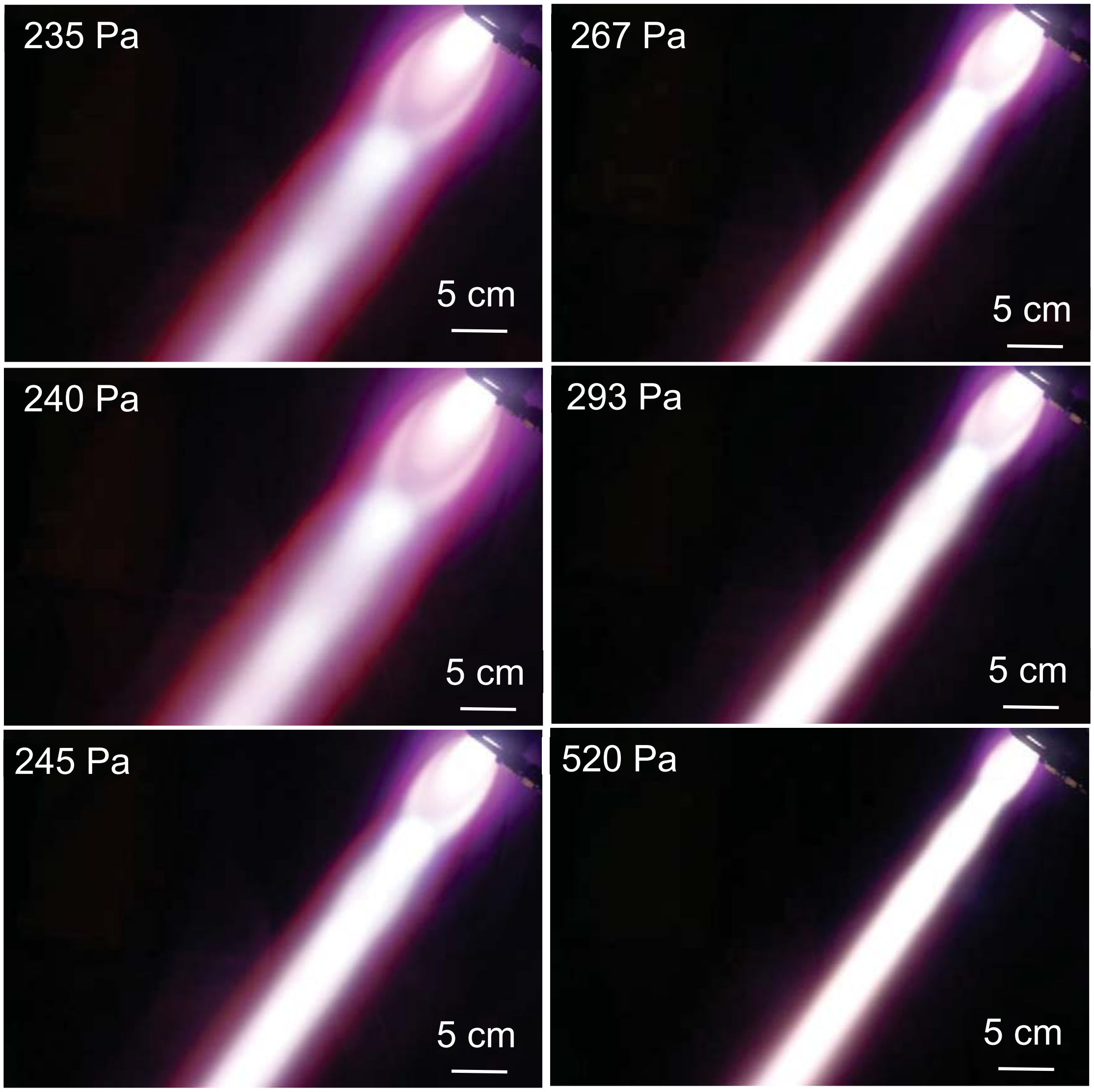

Figure 22: These images show the reduction in plasma expansion with small increases in chamber pressure.

3.2 Very Low Pressure Suspension Plasma Spray Coating Development

This research served to refine the suspension feed system at the TSRL enough to eliminate clogging in spray times up to 30 minutes and powder loading up to 2 vol. %, with this upper limit defined by the capacity and geometry of the pressurized suspension feed vessels, rather than any occurrence of clogging. Substrate thermal management methods were compared via substrate holders with high surface area, internal water cooling, and high heat capacity. Fully adherent coatings were only achieved at pressures below 5 Torr and standoff distances greater than 91 cm, though these two factors were not fully isolated from each other, as the size of the plasma plume has a causal relationship with atmospheric pressure. The maximum coating thickness was limited to ~10 μm before delamination from residual stresses occurred, with density of adherent coatings up to 95%. Deposition efficiency was <10%, contributing to minimum coherent coating thicknesses of ~4 μm. At the thicknesses and densities produced, these coatings were found to be too permeable for effective use as SOFC electrolytes.

Increased plasma enthalpy is a requirement brought on by suspension plasma spray in order to deposit fully molten feedstock. The full range of potential plasma enthalpy could not be tested due to the thermal shock sensitivity of the substrates used in this research. However, across the range of tested parameters, very similar microstructures were produced when coatings adhered to the substrates. While Helium addition did appear to increase plasma enthalpy, the increased overall gas flow rate itself increased the minimum maintainable chamber pressure by 1 Torr, as well as the size of the plasma jet, such that substrates would consistently fall in hotter regions of the plasma than in corresponding Helium free tests. As such, it is suggested that standoff distance should increase with increasing gas flow rate or suspension medium injection, as the plasma plume expansion effect of increased gas flow rate is greater than the size reducing effect of the increased ambient chamber pressure.

The competing concerns in developing VLPSPS coatings were the high plasma enthalpy needed to melt the powder feedstock and the low thermal shock resistance of the YSZ-NiO substrates, necessary for the anode supported SOFC design. The best results obtained were deposits of 4-10 μm, with deposition efficiency <10%. The first generation of coatings, sample set A, produced in May of 2010, varied the powder loading, between 0.25 - 1 vol. %, spray time, from 7-10 minutes, and included a doping trial with 3 and 8 mole % Sc addition. These coatings were created with the relatively high surface area and low heat capacity substrate holder, seen in Figure 8. While tests of multiple standoff distances at a time were thus allowed, it was found that plasma gun power and spray time was limited by the rapid continual heating of the substrates, causing thermal shock. Within the tested standoff distance range of 109-125 cm, no variation in resultant coating microstructure or thickness were found, though closer standoff distances were more prone to thermal shock.

Table 2: Operating parameters for samples created in May 2010 visit to TSRL are shown. Note, all samples used Inframat 40 m^2/g 8 mole % YSZ and 1 wt. % of the dispersant Triton QS-44.

A	A1	A2	A3	A4	A5
Suspension	0.5 vol.%	0.25 vol.%	1 vol.%	3 mol. % Sc	8 mol. % Sc
Chamber Pressure (Torr)	2.4	2.4	2.4	2.4	2.4
Power (kW)	69	69	69	69	69
Gas Mix (Ar,H) (SLPM)	59, 7	59, 7	59, 7	59, 7	59, 7
Spray Time (s)	420	602	600	420	420

The second generation of coatings, sample set B, produced in the summer of 2011, made use of the water cooled substrate fixture, seen in Figure 9, and allowed operation of the plasma gun at the full effective power of 88 kW, with an Ar-H-He gas composition, though its use necessitated decreasing the standoff distance to 91 cm. The water cooled fixture reduced the substrate heating and allowed for steady state operation at < 800 °C, but did not fully eliminate the thermal shock issue.

Table 3: Operating parameters for samples created in summer 2011. All samples used 0.5 vol. % of 40 m^2/g Inframat 8 mole % YSZ and 1 wt. % of PEI.

B	B1	B2	B3	B4	B5	B6	B7
Chamber Pressure (Torr)	2.2	2.2	3.2	3.07	5.7	3.7	3.8
Amps	1800	1800	1800	1800	1800	1200	1500
Volts	49	49	49	44.5	49	45	45
Gas Mix (Ar, H, He) (SLPM)	60, 7, 56	60, 7, 56	60, 7, 56	60, 7, 56	60, 7, 56	60, 7, 56	60, 7, 56
Stand-off distance (cm)	89	89	91	91	91	91	91
Spray Time (s)	255	200	247	181	210	433	424

The third generation of coatings, sample set C, produced in March of 2012, also used an Ar-H-He gas composition, with the water cooled substrate fixture, but focused on lower plasma enthalpy testing parameters, increased deposition time, and the effects of ambient chamber pressure.

Table 4: Operating parameters for samples created in March 2012 visit to TSRL are shown. Note, all samples used 0.5 vol. % of 40 m^2/g Inframat 8 mole % YSZ.

C	C1	C2	C3	C4	C5
Suspension Dispersant	PEI	PEI	PEI	QS-44	QS-44
Chamber Pressure (Torr)	2.35	3.35	5.3	3.65	3.8
Amps	1500	1500	1500	1500	1600
Volts	38	40	42	40	42
Gas Mix (Ar,H,He) (SLPM)	59, 7, 19	59, 7, 19	59, 7, 19	59, 7, 19	59, 7, 19
Stand-off distance (cm)	91	89	91	91	91
Spray Time (s)	486	915	513	513	513

Table 4 Continued:

C	C6	C7	*C8*	C9	*C10*	*C11*
Suspension (vol. %)	1	1	1	1	0.5	0.5
Chamber Pressure (Torr)	3.6	5.3	4.3	4.2	4	4.2
Amps	1500	1500	1500	1500	1500	1500
Volts	40	40.5	47	48	47	41
Gas Mix (Ar,H,He) (SLPM)	59, 7, 19	59, 7, 19	59, 7, 56	59, 7, 56	59, 7, 56	59, 7, 56
Stand-off distance (cm)	91	91	91	91	91	91
Spray Time (S)	671	513	60-120	513	513	300

The fourth generation of coatings, produced in September of 2012, used an Ar-He gas composition, with standoff at 91 and 119 cm. The final variety of substrate fixture was employed, a 12.7 cm diameter, 15.2 cm long stainless steel cylinder, which acted as a heat sink. This fixture, combined with low power preheating of the substrate before deposition, effectively slowed the heating of the substrates as well the cooling rate when the plasma gun was off the substrates, by maintaining chamber vacuum after deposition had ceased. A thermocouple attached to the bottom of the substrates measured heating and cooling at <20 °C/min. The top surface of the substrates is expected to undergo greater temperature variation, but this improvement was sufficient to eliminate thermal shock in all tested configurations. However, as hydrogen was unavailable as a plasma forming gas, the highest plasma enthalpies were not able to be tested.

3.3 Description of Microstructure and Sc-Nitrate Doping Efficacy

Scanning electron microscopy (SEM) was used as a basis for analysis of the effects of standoff distance, powder loading, spray time, and dopant concentration on the microstructure of SPS/VLPPS coatings. The as-sprayed microstructure can be seen in Figure 23, in which the presence of unmelted particles can be seen in the cross section as well as evidence of surface roughness in both micrographs. Figure 25 shows the microstructure of a complete fuel cell after testing, which includes a 2 hour heat treatment at 1200º C. This heat treatment causes some sintering of the electrolyte, though the density is still around 95%.

Unmelted particles in coatings

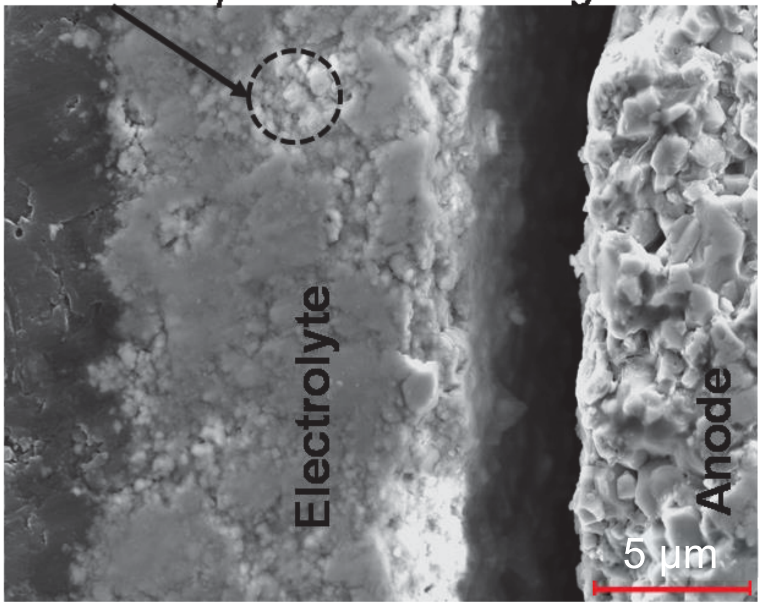

Voids in coating – Surface roughness

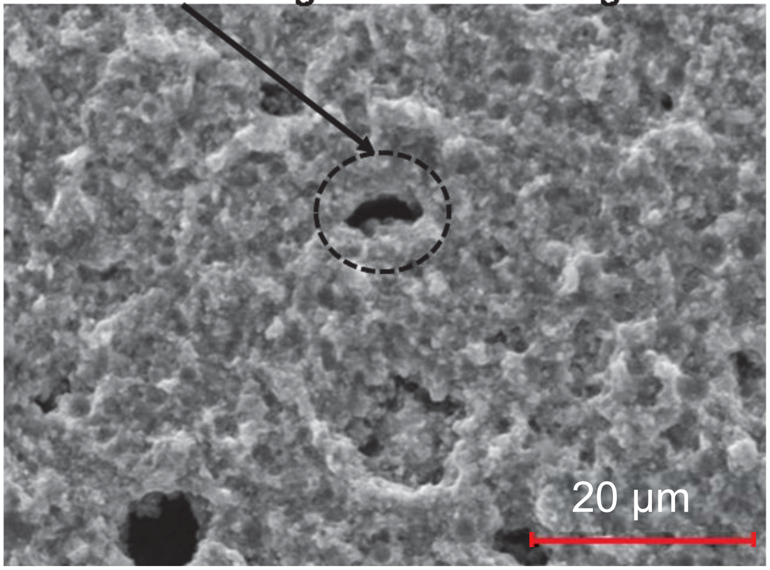

Figure 23: SEM images of the initial microstructures of select VLPSPS coatings are shown. On top is a cross-section of an un-doped 1 vol.% YSZ coating sprayed for 10 minutes at 117 cm standoff. On bottom is a surface image of a 3 mole % Sc-doped 0.5 vol.% YSZ coating sprayed for 7 minutes at 109 cm. Note the presence of un-melted particles in the cross-section image, despite significant density of the coating, and the surface roughness of the bottom image.

The deposition efficiency was calculated based on the coating thickness, suspension powder loading, feed rate, feed time, and the approximate deposition area of the plasma plume, a circle of 15 cm diameter, which accounted to be <10%. Additionally of note is that loose un-adhered powder deposits every surface of the chamber after running the process and particularly collects in the shrouded area around the edge of the substrate. The particle size distribution, as shown in Figure 11, of the 40 m^2/g YSZ VLPSPS powder indicates that approximately 15% are between 0.5-2 microns, with the majority being split between 35% with a mean of 0.1 microns and 50% with a mean of 7. It is assumed the largest particles are primarily agglomerates of the smaller particles, which is supported by their absence from the coatings and the shroud. As can be seen in Figure 24, the shrouded area tends to contain many smaller particles, while the deposited surface is made primarily of particles around 1 micron and neither surface contains indication of splat-like shapes.

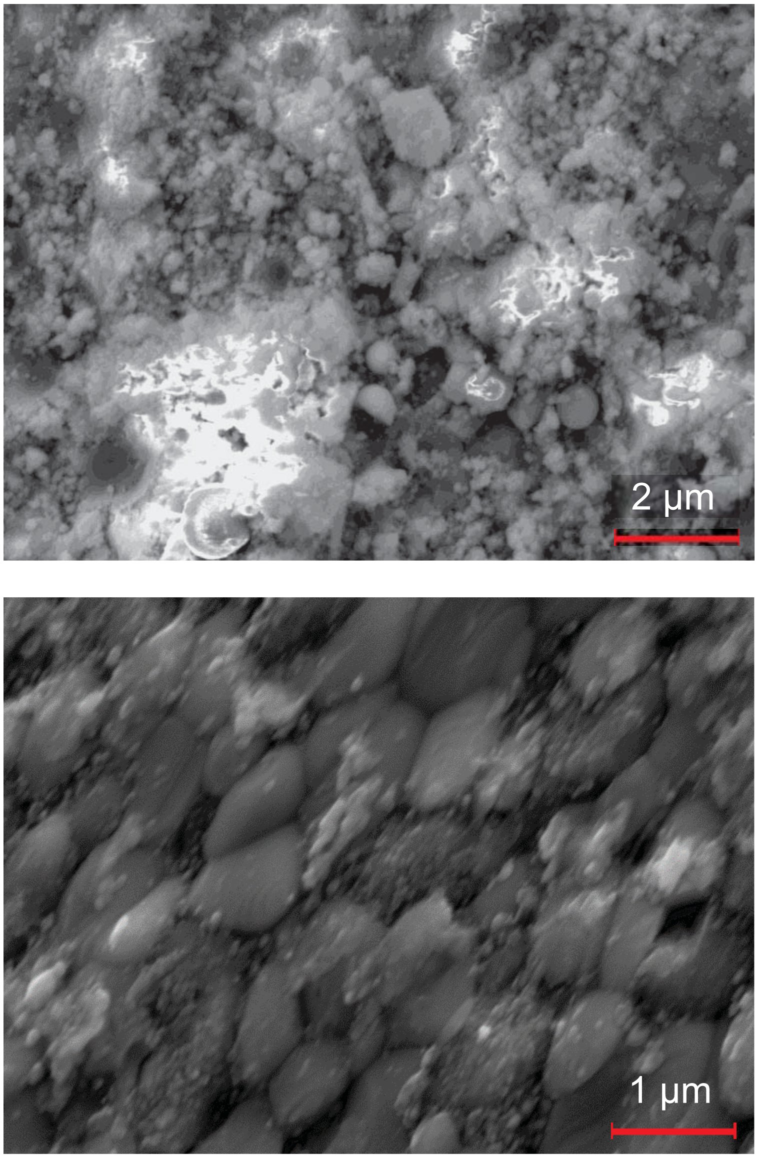

Figure 24: Micrographs of the as sprayed surface of a VLPSPS coating deposited at a 91 cm standoff for 7 minutes, with 0.5 vol.% 40 m^2/g YSZ are shown. The top image shows a shrouded region and the bottom image shows the open deposition surface. Note the scale differences between images.

VLPSPS deposition is particle size selective, in a similar fashion to atmospheric SPS. As particle size goes down, the degree of flow with the carrier gas/plasma increases as momentum vs. surface area decreases. Any moving fluid encountering a surface generates a boundary layer, meaning any particle without sufficient momentum to overcome gas flow will not deposit. Also, the pressure differential between the chamber and the plasma means gas is continually flowing out of the plume along its standoff distance. This selectivity is increased when there is insufficient power to deposit fully melted particles, with selectivity against smaller particle size decreasing with standoff distance as the substrate boundary layer weakens and selectivity against large particle size based on the gun power and suspension medium. Thus, the smallest particles are continually eliminated from the plume via thermophoresis and the continued expansion of the plasma into the vacuum chamber, the largest particles may never melt, and those that remain at high standoff distances are at the lowest temperature of the overall gun to substrate particle stream, but sufficient to both penetrate the boundary layer and 'stick' to the substrate. This does allow for smaller particle agglomerates to melt and combine, but they would have to be mostly re-solidified by the point of deposition, based on the observed microstructures.

The effect of standoff distance on electrolyte coating thickness was shown to be negligible within the tested range 109-125 cm, while surface roughness of the coating can be seen as the limiting factor on the minimum achievable coating thickness. Due to the thin geometries of these coatings, the effect of a few microns of surface roughness served to obfuscate the standoff distance findings. In Figure 25, a complete fuel cell can be see. In Figure 26, a comparison of undoped electrolytes can be seen. In Figure 27 and Figure 28, a comparison of 8 mol. % Sc doped electrolytes is shown at different magnifications. In comparing all 3 sets of images, no distinct difference in thickness can be attributed to stand-off distance.

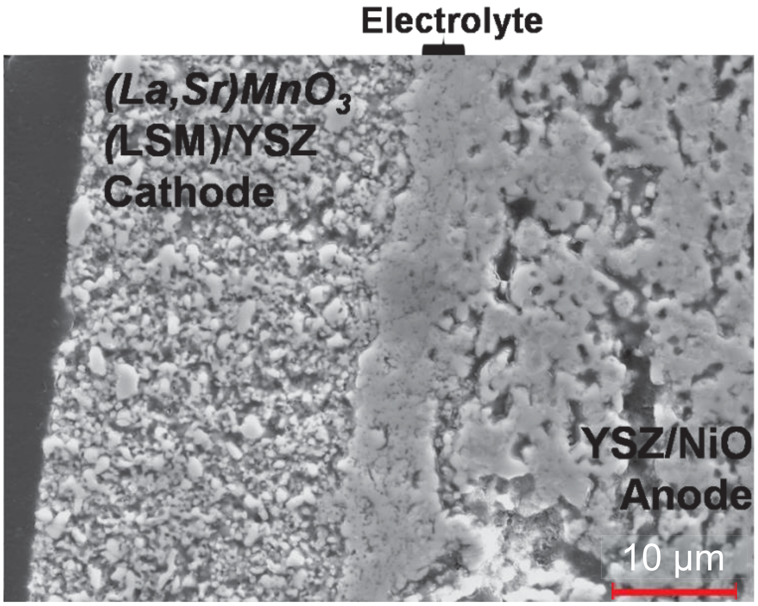

Figure 25: An SEM image of a complete fuel cell after testing is shown. The spray conditions were 8 mol% Sc-doped 0.5 vol% 40 m^2/g YSZ, sprayed for 7 min at 125 cm standoff. Note that in the fuel cell preparation, the coating undergoes a 1200º C - 2 hour heat treatment, which causes some sintering.

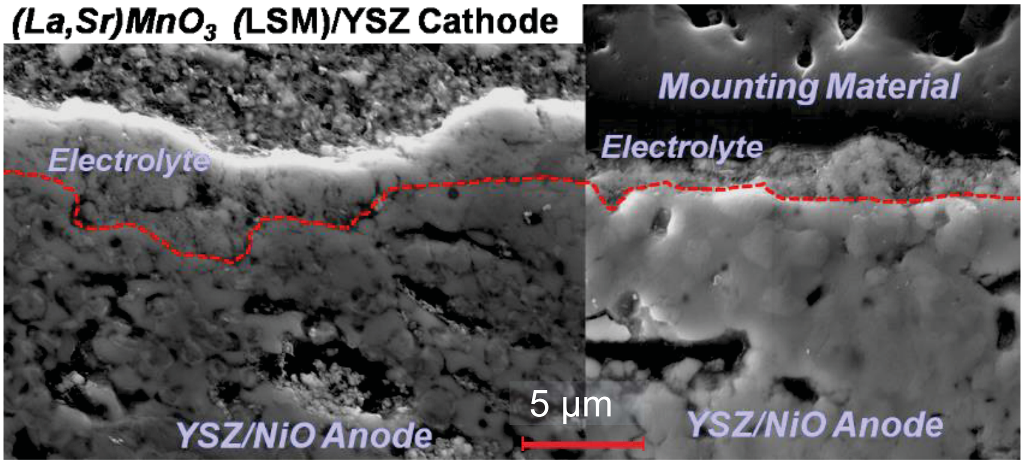

Figure 26: SEM images are shown of 0.5 vol% 40 m^2/g YSZ, sprayed for 7 min at standoff distances of 109 cm (left) and 125 cm (right). While this comparison suggests an increase in thickness for the closer standoff distance, this is attributed to the surface roughness in coating thickness associated with comparing any two individual sections of coatings.

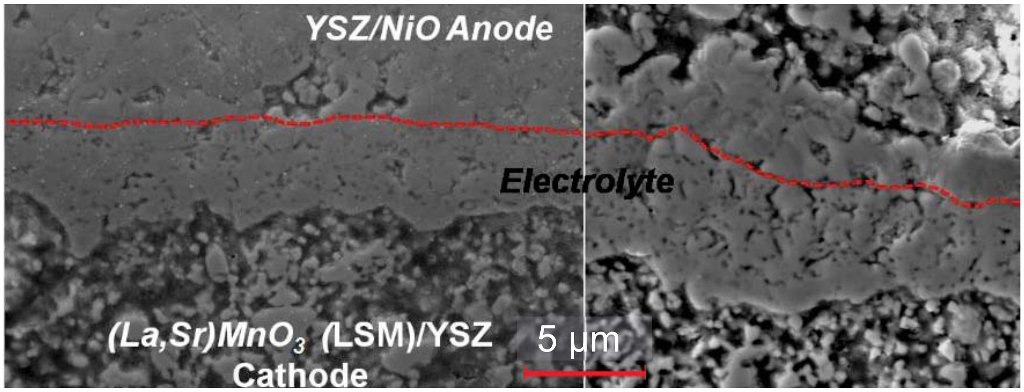

Figure 27: SEM images are shown of 8 mol. % Sc-doped 0.5 vol. % 40 m^2/g YSZ, sprayed for 7 min at a standoff of 109 cm (left) and 125 cm (right). This comparison suggests a slight increase in coating thickness caused by increasing standoff distance within this 16 cm range. However, as seen in Figure 26, this is a byproduct of the bias associated with comparing any two small sections of coatings. See Figure 28 for further evidence of this.

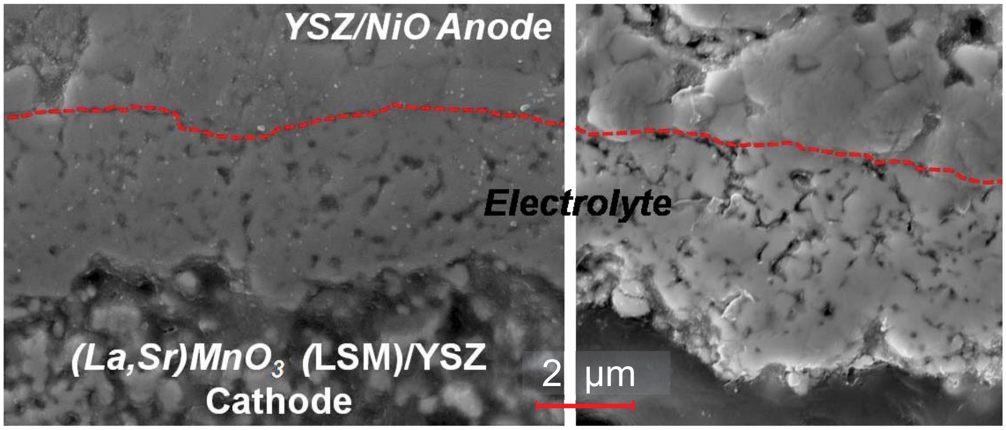

Figure 28: SEM images are shown at higher magnification of the same coatings from Figure 27, 8 mol. % Sc-doped 40 m^2/g 0.5 vol% YSZ, sprayed for 7 min at a standoff of 109 cm (left) and 125 cm (right). This comparison suggests there is no effect on coating thickness caused by changing standoff distance within this 16 cm range. See Figure 26 and Figure 27 for further evidence of this.

The effect of powder loading on electrolyte coating thickness showed a trend that can be approximated as ~1.1 µm/min*vol.%. The surface roughness was shown to increase somewhat with increasing thickness, the extreme of which was only achieved at the highest powder loading, so this effect could not be isolated from powder loading. However, the surface roughness relative to overall coating thickness went down as coating thickness increased. A comparison between 0.25 vol.% and 1 vol.% powder loading, showing the increased coating thickness with increased powder loading, can be seen in Figure 29.

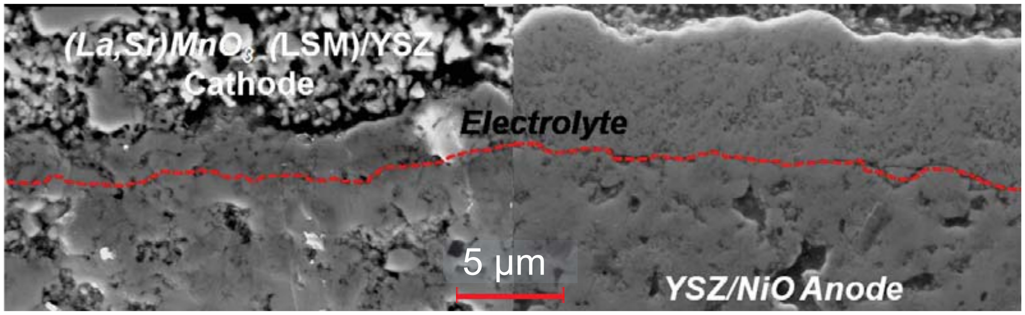

Figure 29: SEM images are shown of 40 m^2/g YSZ at 0.25 vol.% (left) and 1 vol.% (right), sprayed for 10 min at a standoff of 109 cm (left) and 125 cm (right). As expected, this comparison shows a distinct increase in coating thickness associated with increased powder loading.

The microstructure of the 3 mol.% Sc and 8 mol.% Sc-doped electrolyte coatings was found to be very similar and to be relatively indistinguishable from the un-doped coatings, as seen in Figure 30. The true distinguisher of doping was found in the EDS spectrum, as evidenced in the EDS map seen in Figure 31. As such, it is believed that the dopant is in solid solution with the YSZ. It is important to note that the suspension doping does not equal the doping of the resultant coating. Previous doped SPS research has shown a ~50% doping rate [28]. Also, since the net dopant molecule formed is Sc_2O_3, the net doping of the coating is halved. For example, when a suspension is doped with 8 mol. % Sc, the likely net doping of the coating is around 2 mol. % Sc_2O_3. XRD analysis of these coatings can be seen in Figure 32, in which no evidence of a Sc_2O_3 phase can be seen.

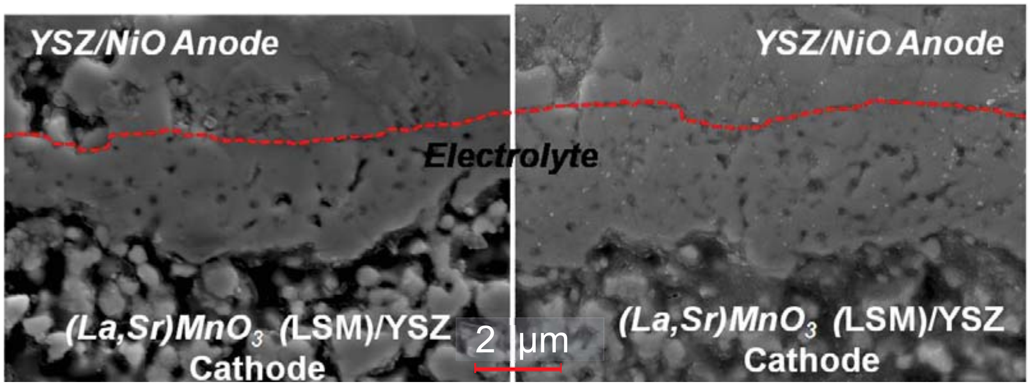

Figure 30: SEM images are shown of 0.5 vol% 40 m^2/g YSZ, sprayed for 7 min at a standoff of 109 cm with doping of 3 mol% Sc (left) and 8 mol% Sc (right). The microstructures are too similar to mark a definitive difference between the doping levels, though fuel cell testing has shown increasing performance with doping.

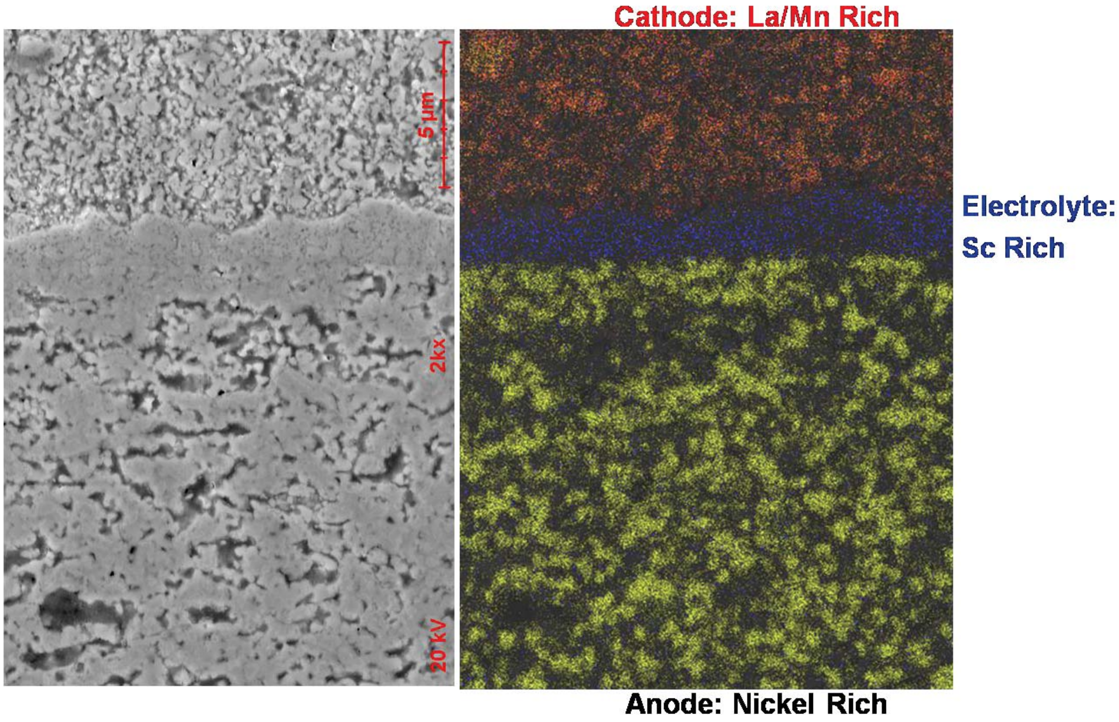

Figure 31: An SEM image and EDS map are shown of a complete fuel cell with an electrolyte created with 8 mol% Sc-doped 0.5 vol% 40 m^2/g YSZ, sprayed for 7 min at 125 cm. The EDS map shows La/Mn in red and Ni in yellow, with the presence of scandium (blue) in the electrolyte clearly visible.

The XRD analysis, in conjunction with EDS measurement of scandium content in doped coatings, supports the supposition that scandium is incorporated into the zirconia lattice during VLPSPS. As seen in Figure 32, below, no Scandia associated peaks are present in the doped samples. The peaks did shift left slightly in the doped samples, as might be expected with the presence of the smaller Sc (in comparison to Y) in solid solution, though this was viewed to be within the error of measurement for these samples, due to the imperfect plane formed by the substrate.

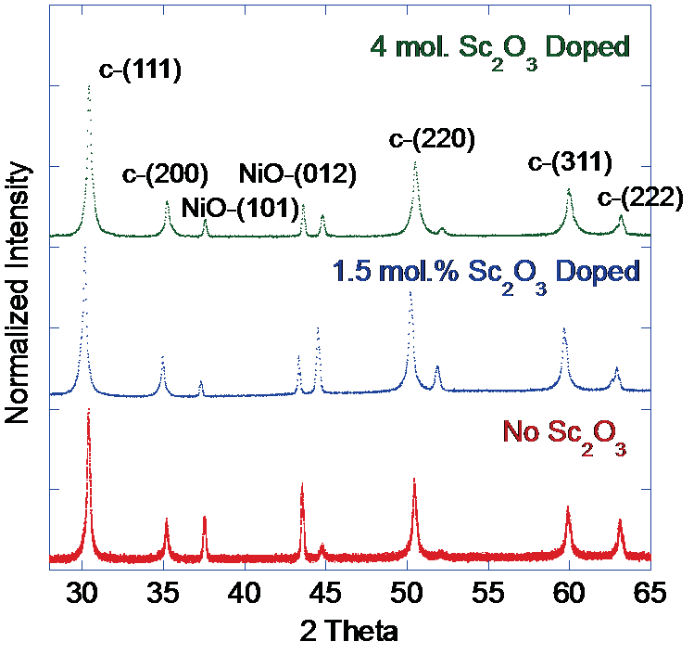

Figure 32: An XRD spectrum comparison between un-doped, 1.5 mol% Sc_2O_3, and 4 mol% Sc_2O_3 electrolyte coatings prepared on a NiO-YSZ substrate is shown. No peaks were associated with a separate Sc_2O_3 phase.

CHAPTER 4. DESCRIPTION AND ANALYSIS OF EPD COATING EXPERIMENTS

This chapter details the processing variables evaluated and experimental conditions employed during successive generations of electrophoretic deposition trials. Analysis of coating microstructures is included when applicable to changes in EPD parameters during subsequent experiments.

4.1. First Generation EPD: Fixture Optimization

The initial fabrication of EPD coatings focused on maintaining as much similarity in suspension composition from the VLPSPS suspensions, while identifying the necessary changes to promote reliable uniform deposition of thin (<10 μm) crack and pore free coatings. The first step was identifying undesirable fabrication artifacts and adapting process fixtures to compensate. The primary fixture issues revolved around the relatively high resistivity of the NiO-YSZ anode substrates and the consequent magnification of electric field strength variability across the surface [70]. This electric field strength variability caused preferential deposition at edges as well as patterned deposition mirroring the shape of the electrode attached to the back of the anode substrate.

Several adjustments were made to reduce the effects of electric field strength variability, centered around the dimensions and nature of the electrode attached to the substrate, as well as the dimensions of the substrate, and the reduction state of the substrate. The electrodes tested included a nanoscale graphite electrode fabricated with an aerosol spray, a ~40 micron thick graphite paste electrode screen printed with a 320 mesh, and a 0.3 mm graphite foil electrode attached with graphite paste. The substrate thickness was varied from a 140 micron 1 layer substrate sintered at 1400 °C for 2 hours to a 1.8 mm 10 layer substrate bisqued at 1000 °C. These tests were carried out for both the NiO and Ni state of the substrate. Reduction of the substrate was carried out at 1000 °C for 2 hours in an Ar/5%H_2 atmosphere. Infiltration of the substrate was done using the deposition suspension or by filling the inner chamber of the fixture holding the substrate. The immersions used for the inner chamber of the substrate fixture were either pure ethanol or ethanol with matching concentration of PEI and/or acetic acid to the external suspension.

The best electrode was found to be the 0.3 mm graphite foil, as it never produced a patterned deposit. Immersion of the substrate for 5 minutes in the depositing suspension before applying a voltage was the best way to get reproducible uniform coatings, with immersion from the inner chamber of the fixture completely preventing deposition. Thin substrates most frequently underwent patterned deposition, when not using the graphite foil electrode, and would lower deposition voltage up to 20%. However, the mechanical strength of the thicker substrates was worth this minor difference, so 10 layer substrates were used as the standard. Reduced substrates allowed EPD at around 10% of the voltage required for the oxidized substrates, with more stable voltage during deposition, a typical difference of a 30V to a 300V average deposition voltage, and were therefore more reliable for the suspension constituent study.

The EPD operating parameters of electrode separation distance, deposition voltage, and deposition current were selected based on established protocols from a literature review and an initial series of constant current and constant voltage tests. Electrode separation was fixed at 1 cm, while the current and voltage parameters were varied within the power supply limits of approximately 0.1 – 1 mA/cm^2. While deposition rate correlates to the applied voltage during EPD, excess voltage is found to lead to turbulent flow near the growing deposit, which leads to increased porosity in the coating [48,49,71]. Therefore, as the end goal of this application of EPD was pore free coatings, the emphasis of this testing was to establish a voltage near to the minimum necessary to drive deposition. Additionally, since current density and voltage change during deposition and the suspension composition itself would be changed during subsequent tests, it was deemed important to set standard conditions well away from the limitations of the power supply [72]. Finally, constant current deposition at 0.47 mA/cm^2 was selected due to the greater independence versus deposit thickness of the constant current deposition mode compared to constant voltage deposition, as discussed in chapter 1.

4.2. Second Generation EPD: Suspension Constituent Study

The role of suspension constituents was analyzed based on a literature review and parametric study of powder loading, powder specific surface area, polyvinyl butyral (PVB) content, polyethyleneimine (PEI) content, and acetic acid content, as described in Table 5 [73,74,75,76]. The deposits formed in the suspension constituent analysis utilized a fixed electrode separation of 10 mm, with constant current deposition at 0.47 mA/cm^2. Each deposition was carried out with 300 mL of suspension, which was calculated to result in <1% depletion of the suspension constituents over the course of deposition, based on measurements of deposit yield and thermogravimetric analysis (TGA) measurements of deposit constituents. A TGA plot of a coating deposited from a suspension of 0.25 vol. % 13 m/g^2 YSZ, 1 wt. % PEI, and 8 g/L PVB, can be seen in Figure 33. The TGA revealed that the as deposited coating is approximately 97.5 weight % YSZ, which amounts to approximately 88 vol. % YSZ, not counting porosity, with the remainder being a combination of PEI and PVB. Assuming a standard drying shrinkage of 10-15% and a particle packing density of 60%, this means the combined PEI and PVB content in the liquid phase of the growing deposit is between 14 -16 vol. % and 18 -19 wt. %, which represents a very large increase over the combined 2 wt. % they represent in the bulk suspension.

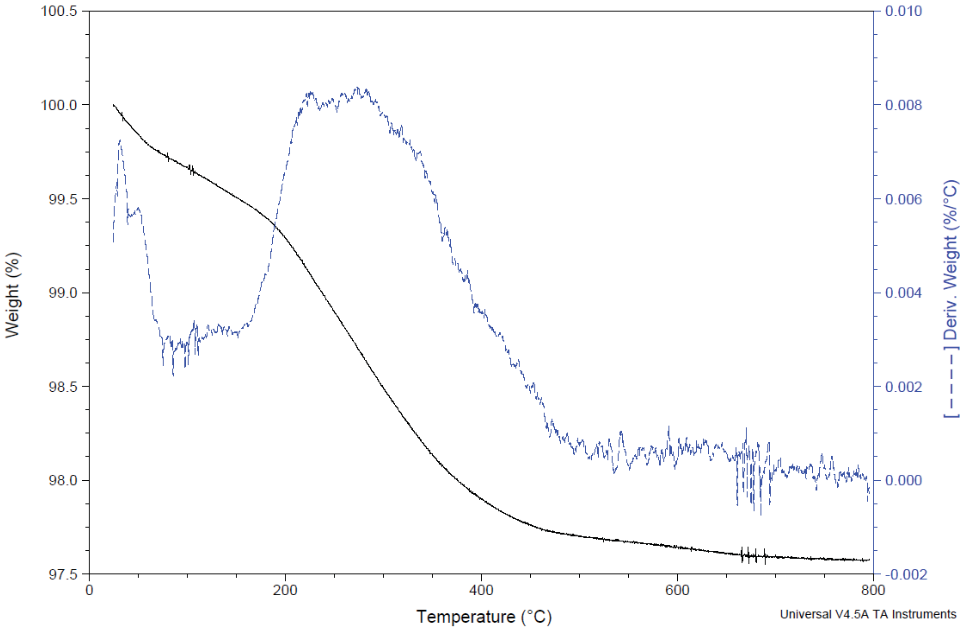

Figure 33: This figure shows thermogravimetric analysis of an electrophoretically deposited coating from a suspension of 0.25 volume % 13 m^2/g YSZ, 1 weight % PEI, and 8 g/L PVB, in ethanol, after drying for 24 hours.

Table 5: The EPD suspension constituent testing regime is shown. All coatings were created at 0.47 mA/cm^2 for 10 minutes at 10 mm electrode separation, with the voltage response recorded with an Agilent 34401A Digital Multimeter.

YSZ (vol. %)	Specific Surface Area	PEI (weight %)	PVB (g/L)	Acetic Acid (M)
0.25	13	1	8	0
0.25	13	1	8	10^{-2}
0.25	13	1	8	3×10^{-2}
0.25	13	1	4	0
0.25	13	1	2	0
0.25	13	1	0	0
0.25	13	2	8	0
0.25	13	0.5	8	0
0.5	13	1	8	0
2	13	1	8	0
0.25	40	1	8	10^{-2}
0.25	40	1	8	0
0.25	40	1	4	0
0.25	40	1	2	0
0.25	40	1	0.75	0
0.5	40	1	0	0

The primary metrics of deposition quality analysis were crack presence, deposit adherence, deposit uniformity, and deposit porosity. The deposition quality was determined based on a tiered analysis, focusing first on the elimination of cracking as the most serious and obvious issue faced. Also, some suspension compositions either resulted in no coating formation or such limited adherence that the coating did not survive removal from the suspension. Another feature of poor deposit adherence would be striations in the coating perpendicular to the axis of removal from the suspension, indicating partial delamination and flow of the deposit while in the wet state immediately upon removal from suspension. This effect was distinct from “mud-crack” drying from capillary drying stresses, as the cracking would only occur with fast removal of the substrate from the suspension that could visibly be seen to cause delamination and flow of coatings. An example of these striations can be seen in Figure 34. Initially, these striated or cracked deposits were also integrated into SOFCs and their performance was tested, but they were found to be nonfunctional as electrolytes. These striations did not occur with every test, with thinner depots being more resistant. However, increased removal rate was qualitatively found to lead progressively from uniform deposits, to striated deposits, and finally to completely failed deposits in which the remnants of the deposit were seen to flow with the direction of the withdrawal. A removal rate of roughly 2 cm/min from the EPD suspension seeming to eliminate this effect, but acetic acid addition to the suspensions completely eliminated it without the need to add equipment to the EPD fixture to facilitate this slow removal and was thus the preferred solution.

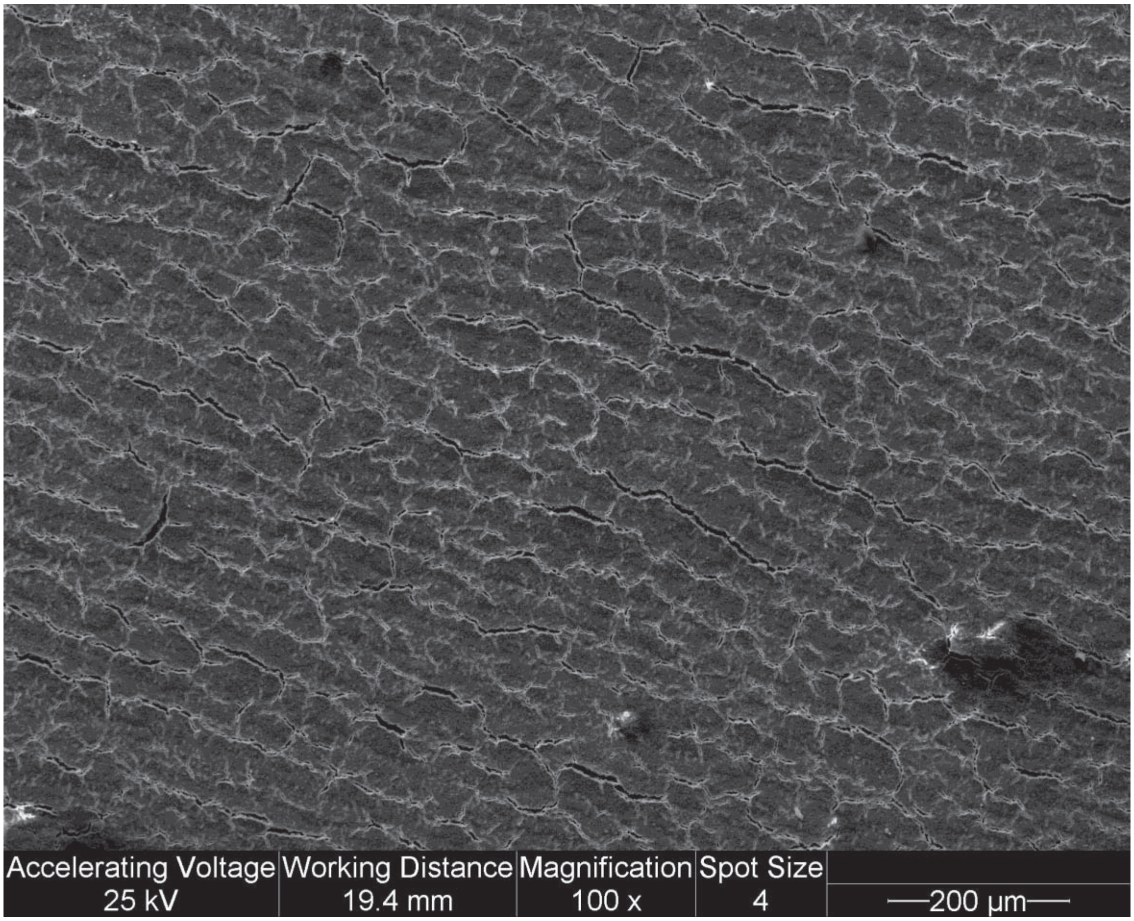

Figure 34: A topographic micrograph is shown of an EPD coating formed from 0.25 vol. % 13 m^2/g YSZ, 1 wt. % PEI, and 8 g/L PVB. Note the parallel spaced cracks, which are an artifact of the process of removing the coating from the EPD suspension.

In addressing deposit cracking, the key suspension properties were found to be the specific surface area of the particles and the presence of the binder polyvinyl butyral (PVB). The 40 m^2/g YSZ powder based suspensions all showed “mud crack” surface topographies, with the incidence of cracking being reduced by decreasing deposit thickness and increasing PVB content, but not consistently eliminated, as illustrated in Figure 35 & Figure 36.

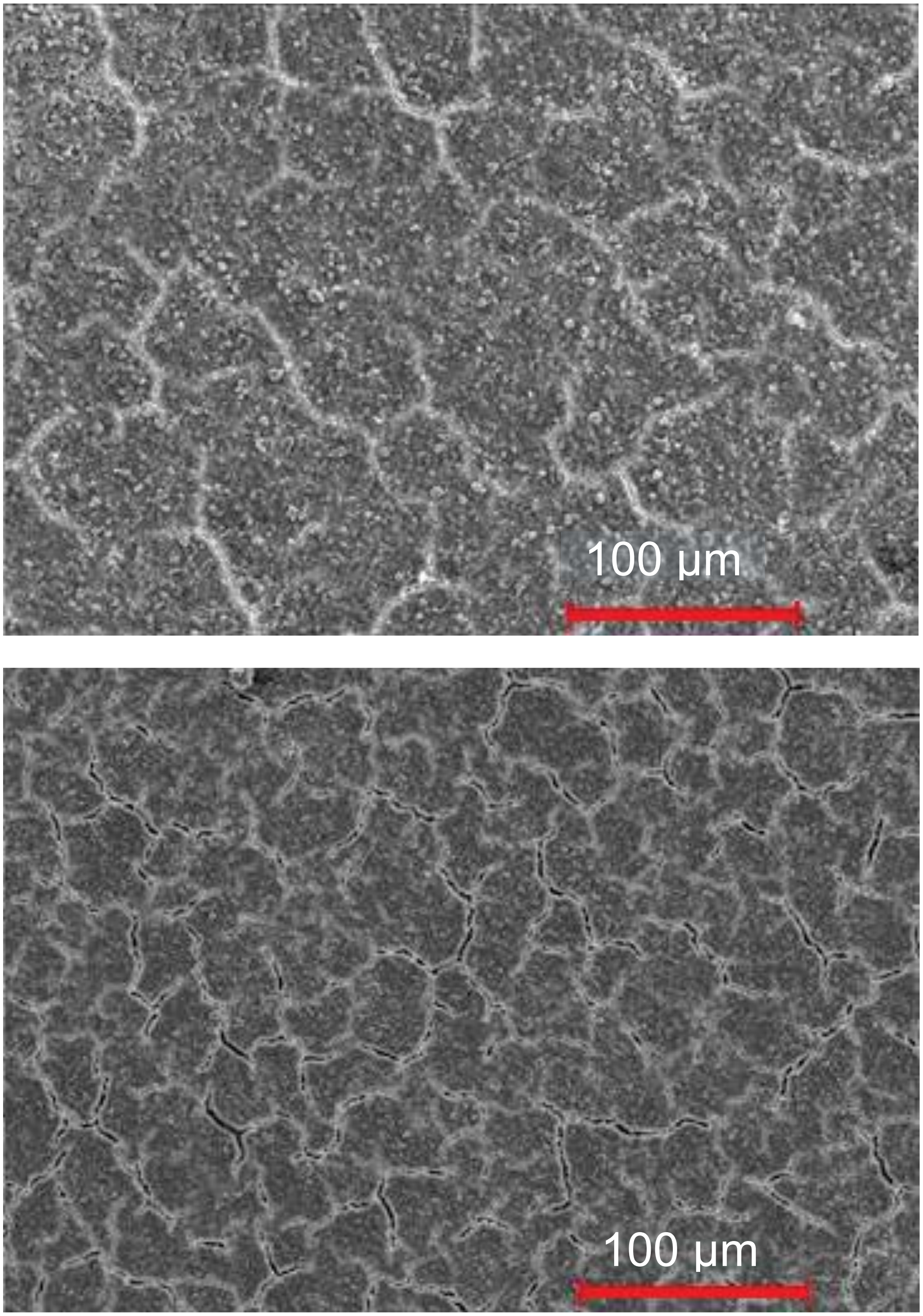

Figure 35: Topographical micrographs are shown of deposits from 0.25 vol. % 40 m^2/g YSZ, 0.75 g/L PVB, and 1 wt. % PEI. The top image is as deposited, while the bottom image is after sintering for 2 hours at 1400 °C.

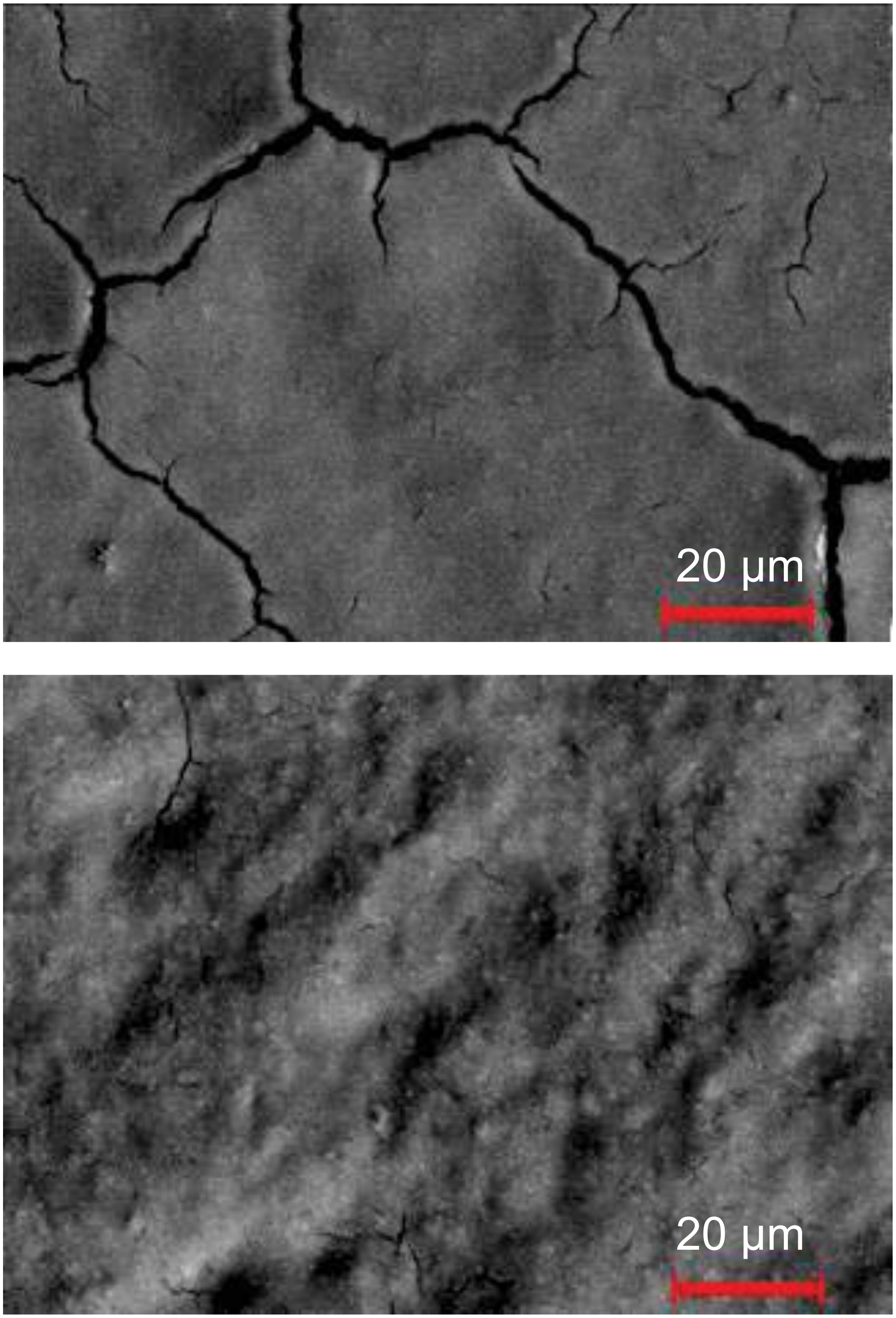

Figure 36: Topographical micrographs are shown of deposits with 0 PVB (top) and 2 g/L PVB (bottom) with the remaining constituents of 0.25 vol. % 40 m^2/g YSZ and 1 wt. % PEI.

With the 13 m^2/g YSZ powder based suspensions, cracking was eliminated with the addition of 4 g/L of PVB. The 8 g/L PVB content of 13 m^2/g showed the same effect on eliminating cracking, without any discernible change in other deposit properties, and was used for later testing as a safeguard against the increased drying stresses associated with deposition of thicker coatings. While the focus of this study was thin, <10 μm, deposits, deposits up to 2 mm were created with this suspension composition, none of which exhibited any occurrence of cracking.

The role of PEI content on the suspension was first to provide suspension stability, but it was also found to act as a charge carrier during EPD, such that concentrations in excess of that necessary for stability caused reduction of deposition voltage and indication of preferential deposition of PEI over YSZ. At the highest tested concentration of 2 wt. % PEI, the deposit lacked YSZ, consisting of the polymer constituents of the suspension in irregular, rough deposits.

The acetic acid content of the suspension in electrophoretic deposition forms part of the diffuse boundary layer around particles and also acts as a free ion charge carrier. In its role as a free ion charge carrier, the addition of acetic acid lowers the suspension resistivity, thus reducing deposition voltage, while also acting as a parallel circuit to that of the ions directly involved in electrophoretic deposition. This effectively leaches current from the deposition process, which is a negative factor in increasing acetic acid concentrations that can lead to prevention of electrophoretic deposition. Acetic acid was found to reduce the initiation period for deposition, allowing uniform deposits to form in as little as 1s at 8 V. Without acetic acid, it took at least 2-3 minutes before an adhered coating would form at a deposition voltage around 30-40 V. It may be that acetic acid free deposits grow similarly, but that their inter-particle repulsion remains slightly too high after deposition and thus they have insufficient cumulative bond strength for adhesion outside of the suspension. As these acetic acid free deposits grow thicker, the relative effect of the suspension flow along their surface lessens to the point where they maintain adhesion or there is always some sacrificial part of the coating at the surface that is removed. In these thicker deposits, as seen in Figure 37, the thickness and microstructure are virtually the same within the range of acetic acid tested.

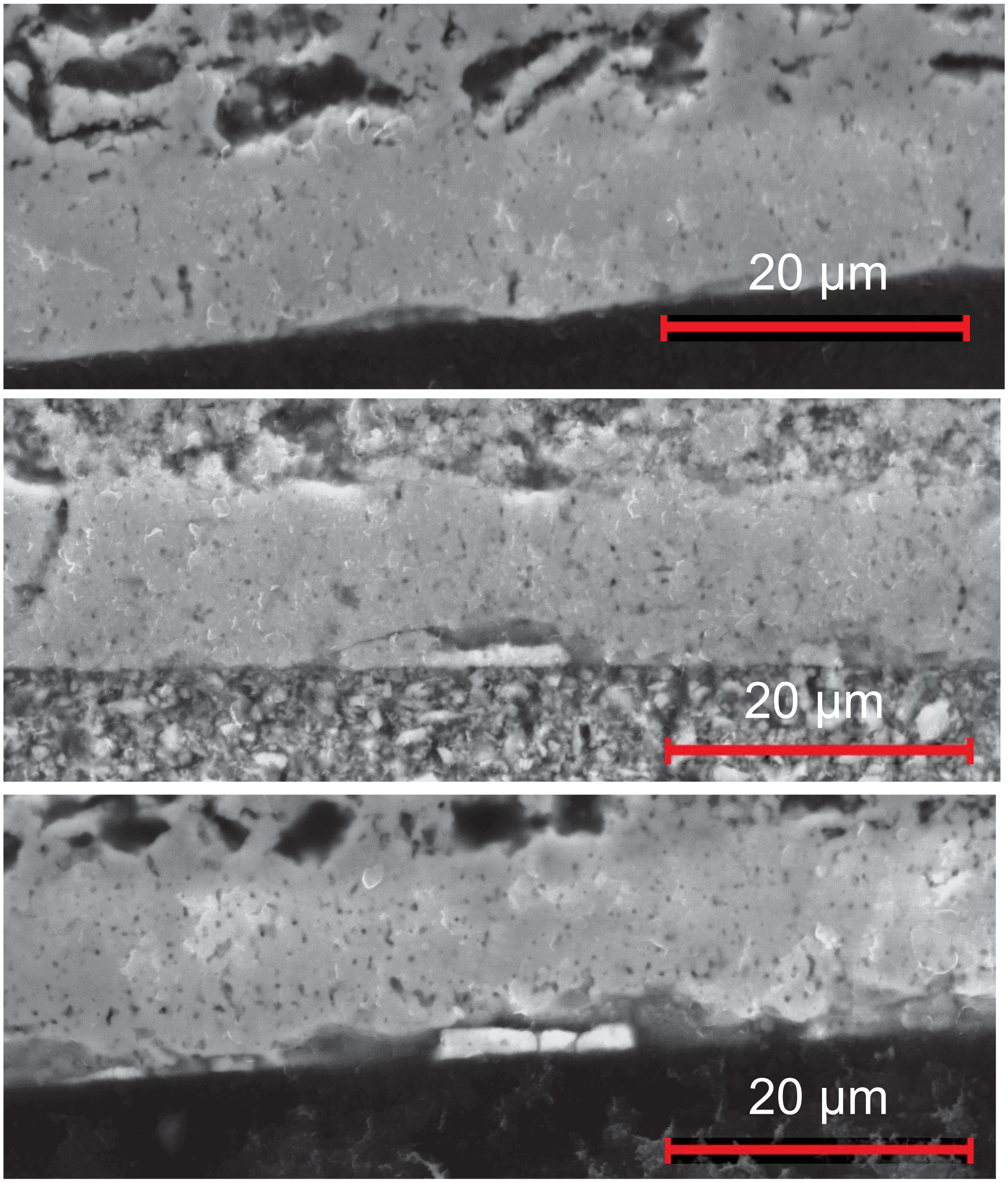

Figure 37: Micrographs are shown of polished cross sections of EPD coatings deposited for 10 minutes with varying acetic acid content of none (top), 10^{-2} M acetic acid (middle), and 3 x 10^{-2} M acetic acid (bottom). The rest of the constituents of the suspensions were constant, with 0.25 vol. % 13 m^2/g YSZ, 1 w. % PEI, and 8 g/L PVB.

Another key in explaining the initiation period of EPD is related to the suspension concentration increase that occurs near the electrode after the onset of deposition, which results in an effective increase in particle loading as well as changes in ion concentration and thus inter-particle repulsion. Ultimately, the boundary between deposit and suspension is a nearly continuous one, with particle concentration increasing to the point of contact and continued shifting of connected particles near the surface towards local increased electric field strength. The degree to which this happens is dependent on the stability of the suspension and the change in stability versus distance from the electrode and the growing deposit surface, as shown by Sarkar et al. [73]. While the concentration of acetic acid was below the detectability of the TGA measurements performed, the effect of concentrating materials from the boundary layer confirmed by the TGA is expected to affect acetic acid as well. Also, the short deposition time means the suspension deposited from close to its equilibrium state, with minimal time allowed for suspension concentration to build up around the electrode, though the local shift in free ion concentration would occur at a faster rate than that of the particles themselves as their charge to mass ratio is much higher. These results indicate that the key effect of the acetic acid is to increase the inter-particle attraction within the deposit without negatively impacting the stability of the particles in the suspension.

The suspension with the greatest reproducibility of uniform and well adhered deposits from the parametric study consisted of 0.25 vol. % YSZ, with a specific surface area of 13 m^2/g, 1 weight % PEI, 8 g/L PVB, and $3x10^{-2}$ M acetic acid. An example of EPD coatings made from this composition can be seen in Figure 38, depicting a 43 micron thick un-sintered EPD coating and a 27 micron thick EPD coating sintered at 1400 °C for 2 hours. In Figure 39, an EPD coating can be seen at multiple scales, comparing both polished and fractured surfaces. Sintered deposits reached 97% density, but coalesced pores were present after sintering.

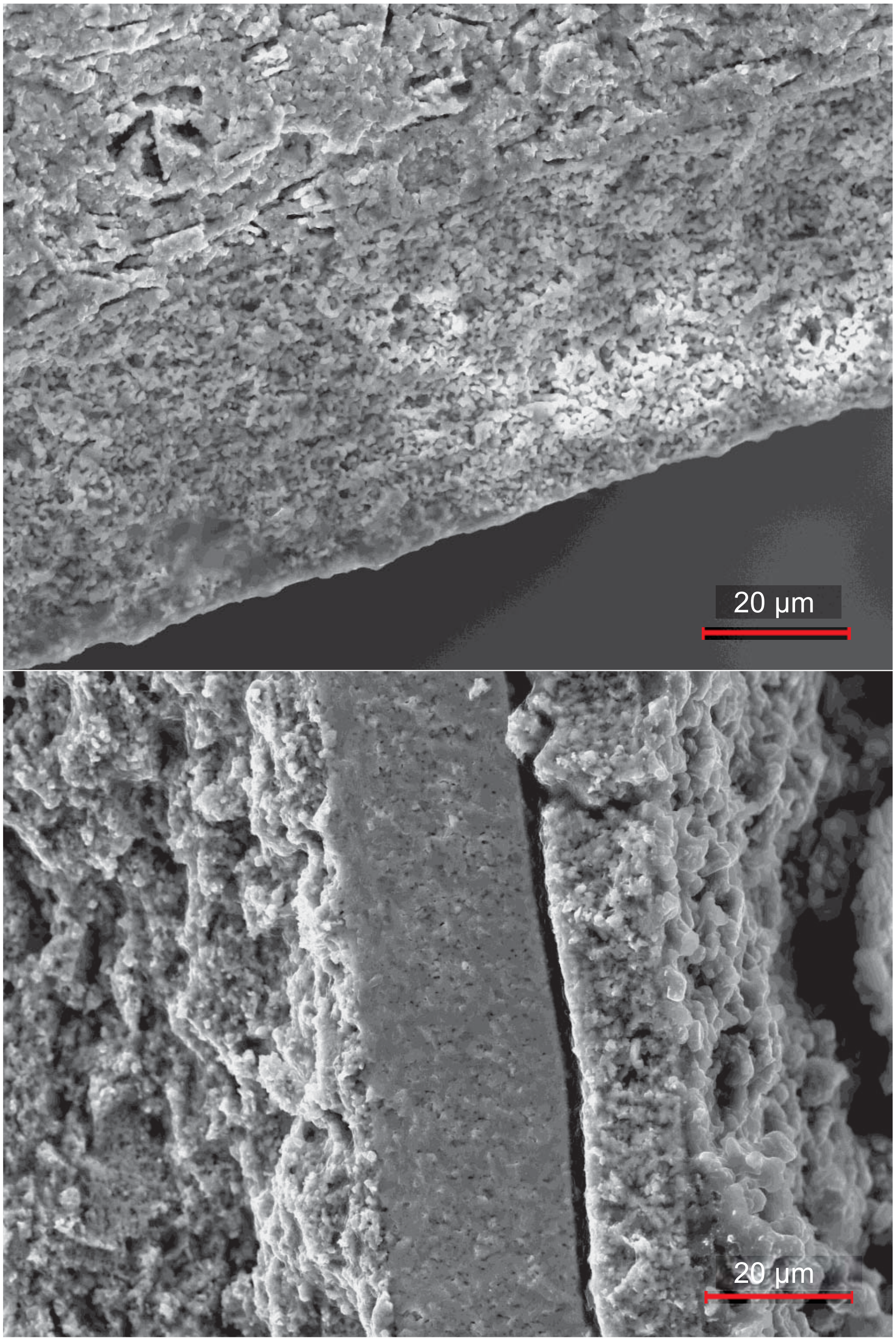

Figure 38: Micrographs are shown of as deposited (top) and post sintering (bottom) of deposits formed at 0.47 mA/cm^2 for 10 minutes from suspensions of 0.25 vol. % 13 m^2/g YSZ, 1 w. % PEI, 8 g/L PVB, and 3 x 10^{-2} M acetic acid.

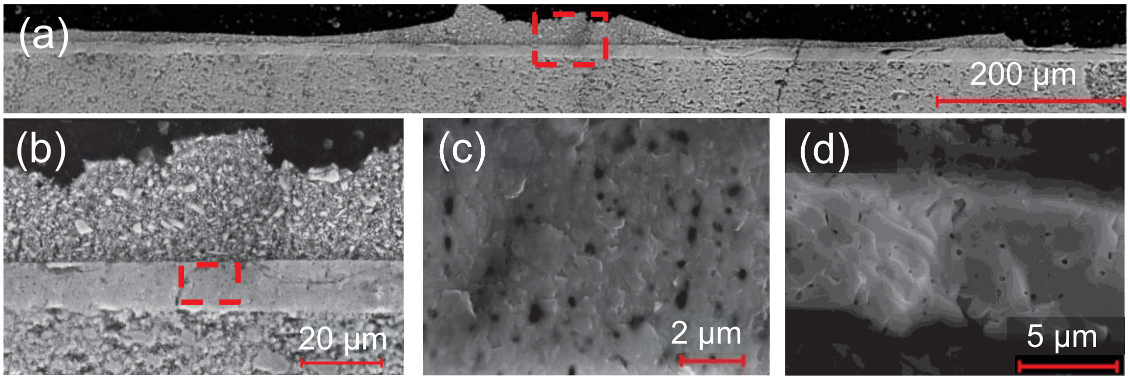

Figure 39: A series of micrographs is shown, at progressive scales, of the same SOFC, with a-c being polished samples and d being a fracture surface. The sample was produced via 0.25 vol. % 13 m^2/g YSZ, 1 wt. % PEI, 8 g/L PVB, and 3×10^{-2} M acetic acid deposited for 10 minutes at 0.47 mA/cm^2.

The final step in preparation for deposition of bilayer YSZ-GDC was to further explore the deposition initiation and growth over time in order to minimize electrolyte thickness. Surface roughness is a key factor in establishing minimum deposit thickness, so topographic micrographs were taken for deposits formed over 1.5, 30, and 60 seconds, as seen in Figure 40. These topographic images showed that shorter deposition times produced less surface roughness, so the primary limitation on thickness is the porosity of the coating, which was found to lead to permeable coatings when <5 microns thick.

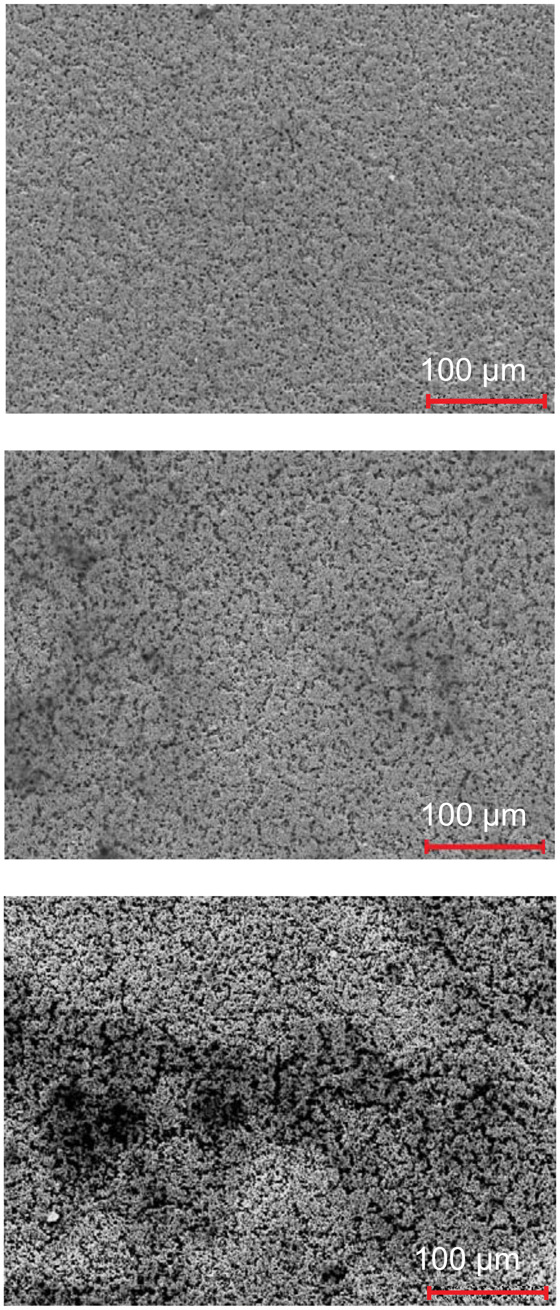

Figure 40: Surface topographies are shown; note increasing surface roughness with deposition time between 1.5s, 30s, and 60s, from top to bottom, respectively. Deposits formed at 0.47 mA/cm^2 from suspensions of 0.25 vol. % 13 m^2/g YSZ, 1 w. % PEI, 8 g/L PVB, and 3 x 10^{-2} M acetic acid.

4.3. Third Generation EPD: Bilayer YSZ-GDC Electrolytes

Bilayer electrolytes were produced from GDC and YSZ, with the objective of using the YSZ layers as barriers against the low pO_2 atmosphere at the anode, and utilizing the lower temperature ionic conductivity of the GDC [77,78,79,80,81,82,83]. The GDC suspension composition was selected based on the findings from the YSZ suspension constituent study, though it was found that the acetic acid was not necessary for GDC coating adherence, so the bilayers were all formed with suspensions of 0.25 vol.% GDC, 1 wt. % PEI, and 8 g/L PVB. The ideal thickness of each layer of the bilayer was initially estimated based on a study of deposition time of each YSZ electrolyte versus open circuit voltage in a functional solid oxide fuel cell, as discussed further in chapter 5 and Table 7. From these results, select combinations of YSZ and GDC were then tested. The idea was that the best YSZ layer would be one that on its own could not provide full theoretical open circuit voltage. As the deposits were crack free, the lack of full open circuit voltage was attributed to the porosity in the coating allowing hydrogen permeation and thus reducing the electrical potential. This partial open circuit voltage was indicative of the YSZ layer operating in the lowest pO_2 environment and thus with an additional layer of GDC, the theoretical open circuit voltage could be achieved without exposing the GDC to a reducing atmosphere, while also mitigating the effect of reduced low temperature ionic conductivity in the YSZ layer.

Bilayer deposits were attempted via sequential wet deposition as well as with an intermediate bisque of the YSZ layer for 2 hours at 1000 °C in an $Ar/5\%H_2$ environment. An example of the sequential wet deposition can be seen in Figure

41, with accompanying EDS map. Unfortunately, it was difficult to define the transition between YSZ and GDC, just their relative presence on each side of the electrolyte. Both methods resulted in functional SOFCs, but the intermediate bisque produced denser deposits, with higher power densities and open circuit voltage, as discussed in chapter 5. A micrograph of a YSZ-GDC bilayer produced with sequential wet deposition can be seen in Figure 41.

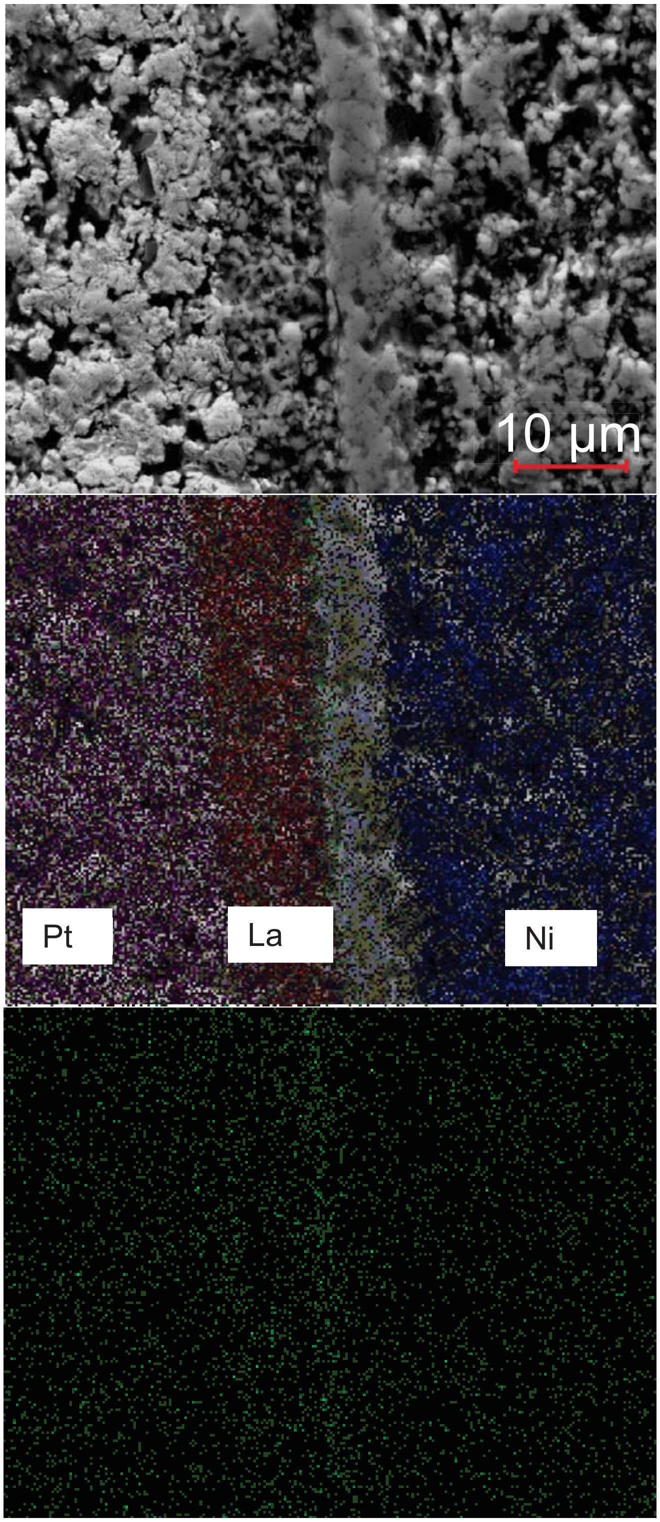

Figure 41: A micrograph and EDS map is shown of a YSZ-GDC bilayer. Cerium is shown in green, at a minimal detectable level, while Pt, La, and Ni are unique elements in the electrode, cathode, and anode, respectively, shown for contrast.

4.4. Fourth Generation EPD: Sc-Nitrate Doped Suspension Based Coatings

The last set of SOFC electrolytes were produced to evaluate the effectiveness of doping electrophoretic deposits with metal salts as a means of composition control in the final deposit. Varying concentrations of scandium nitrate in the electrophoretic deposition suspensions were used as a means of evaluation. The main concerns over the effectiveness of this method were the yield of scandia in a deposit, relative to the scandium nitrate concentration in the electrophoretic deposition suspensions, as well as the effectiveness of the scandia incorporation into the YSZ lattice. The nature of electrophoretic deposition is that any scandium nitrate deposited must initially exist on the surfaces of the deposited particles and thus must decompose to scandia and diffuse into the particles via subsequent heat treatment. EDS of resultant deposits sintered for 2 hours at 1400° C can be seen in Table 6, showing a doping efficiency of 54%, representing the proportion of scandium in the deposit relative to the initial concentration of scandium, relative to YSZ, in the suspension. However, as further discussed in chapter 5, SOFC testing indicates that the scandium doesn't diffuse into the YSZ enough to disperse evenly, so the EDS is likely over counting the predominantly surface scandium content.

Table 6: EDS results for a deposit formed with a 16 mole % Sc-nitrate doped suspension are shown, indicating a doping efficiency of 54%.

Element	Wt%	At%	Z	A	F
Y L	16.9	16.5	0.9958	0.9512	1.0004
Zr L	78.3	74.3	0.995	1.0032	1.0005
Sc K	4.8	9.3	1.0986	0.5711	1
Total	100	100			

CHAPTER 5. DISCUSSION OF SOFC PERFORMANCE AND PROCESSING RELATIONSHIPS

In this chapter the coatings produced via very low pressure suspension plasma spray and electrophoretic deposition are analyzed with respect to their performance characteristics as electrolytes within a complete solid oxide fuel cell. The performance was characterized via comparison of microstructure, potentiodynamic response, and impedance spectroscopy. They key metrics were electrolyte thickness, electrolyte density, peak power density of the SOFC versus temperature, and total interfacial resistance of the SOFC versus temperature. The two deposition processes produced similar microstructures, with densities above 95%, and were both used to fabricate <10 μm electrolytes. There were a limited number of viable VLPSPS samples, though the feasibility of doping with metal nitrates to achieve compositional mixing sufficient for electrochemically active electrolytes was confirmed.

The similar nature of EPD microstructures to the VLPSPS microstructures allows for some extrapolation of the latter’s capabilities, if further explored, based on the EPD findings here reported. The two most significant distinctions between these two processes was found to be that (1) VLPSPS coatings achieve their density in the as-sprayed state, without requiring further heat treatment, as needed with EPD and (2) dopants from metal nitrates in suspension are incorporated into the lattice structure of the host particle feedstock during VLPSPS, but are only present on the surface of particles within EPD coatings.

5.1. Very Low Pressure Suspension Plasma Spray Electrolytes

The fuel cell testing of the electrolyte coatings has shown improvement in power density with scandia doping, however an initial flaw in the testing methodology caused overly thick electrodes that resulted in low current densities, negating the impact of these results. Standard fuel cells, consisting of the same YSZ-NiO anode support, 6-10 μm 8 mole % YSZ electrolyte, and LSM based cathode were purchased from Fuel Cell Materials, Inc in an effort to compare results, given this limitation, and as a method to identify the testing flaw. This led to an improvement in the testing procedure, but limited access to the VLPSPS equipment at Sandia National Laboratories' Thermal Spray Research Laboratory and mechanical breakdowns of the equipment barred further efforts in VLPSPS electrolyte fabrication research. However, with the improvement of the testing procedure came validation of the open circuit voltage (OCV) measurements of all tests. This consistently showed the SOFCs produced from the VLPSPS electrolytes to be of low quality at the evaluated thicknesses, while suggesting the characteristic porosity of the process would be suited for thicker electrolytes of around 15+ μm to achieve impermeability to hydrogen.

In Figure 42, the results are shown of the performance comparison of the standard cell and the best VLPSPS fuel cell produced, when tested using the initial low current density method. The standard cell that was tested was rated for 800 mW/cm^2 peak power density at 800 °C, but clearly suffers from low current density in these tests, with a peak power density of 40 mW/cm^2. However, the open circuit voltage of 1.1 V matches expected results. Within this significant caveat of all around low current density, the power density performance of the VLPSPS electrolyte is comparable to the standard cell. An important point to note is the more accurately measured OCV, which is the y-axis intersection of the IV curve, representing the electromotive force of the reaction, which should be around 1.1V, as the standard cell is. At an OCV of 0.7 V, the VLPSPS electrolyte suffers an inherent disadvantage in achieving high power densities.

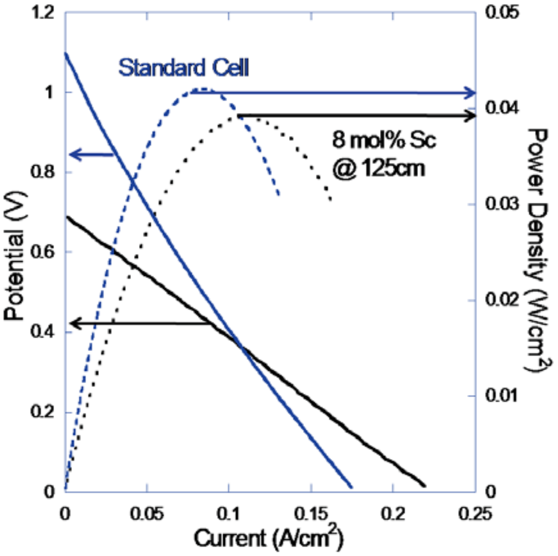

Figure 42: Potentiodynamic testing results are shown comparing an 8 mol% Sc doped 0.5 vol. % 40 m^2/g YSZ, sprayed for 7 min at a standoff of 125 cm, to a standard cell, made from similar components, including a YSZ electrolyte, purchased from Fuel Cell Materials, Inc.

The OCV of VLPSPS electrolyte SOFCs was found to be dependent on the electrolyte thickness, with the thickest coating, ~11 μm, having 0.93V. This thickness relationship is attributed to porosity in the coating allowing for electrolyte permeability at lower thicknesses. Attempts were made to fabricate thicker coatings, but delamination was a limiting factor along with increased thermal load due to increased deposition time that lead to thermal shock of the substrates.

5.2. Electrophoretically Deposited YSZ Electrolytes

Electrolyte coatings produced using electrophoretic deposition performed comparably to similar coatings reported by Hosomi et al. [55] and Besra et al. [54]. The highest stable power density achieved was approximately 440 mW/cm^2 at 800 °C for a cell consisting of a NiO/YSZ anode, screen printed LSCF cathode, and a 7.8 μm thick YSZ electrolyte deposited for 10 minutes at 0.47 mA/cm^2 from a suspension of 0.25 volume % YSZ, 1 weight % PEI, 8 g/L PVB, and 10^{-2} M acetic acid, in ethanol and sintered for 2 hours at 1400°C. At 800 °C, the total interfacial resistance of this cell, as measured via impedance spectroscopy, was 0.7 Ω·cm^2. Another cell, fabricated under the same parameters, but resulting in a less dense 4.7 μm thick YSZ electrolyte, as measured via SEM cross section, reached a power density of 520 mW/cm^2 at 800 °C, with a total interfacial resistance of 0.14 Ω·cm^2, but had a poor open circuit voltage of 0.7 V and suffered performance degradation over the initial 24 hours of operation. While this was the highest measured peak power density, the low open circuit voltage and increased porosity of the electrolyte indicated permeability of the electrolyte, thus the effective partial pressure drop across the electrolyte was decreased versus ideal. However, the diffusion path of oxygen ions in the electrolyte was also shorter, which may have compensated for the lower open circuit voltage. Micrographs of the three best performing cells can be seen in Figure 43.

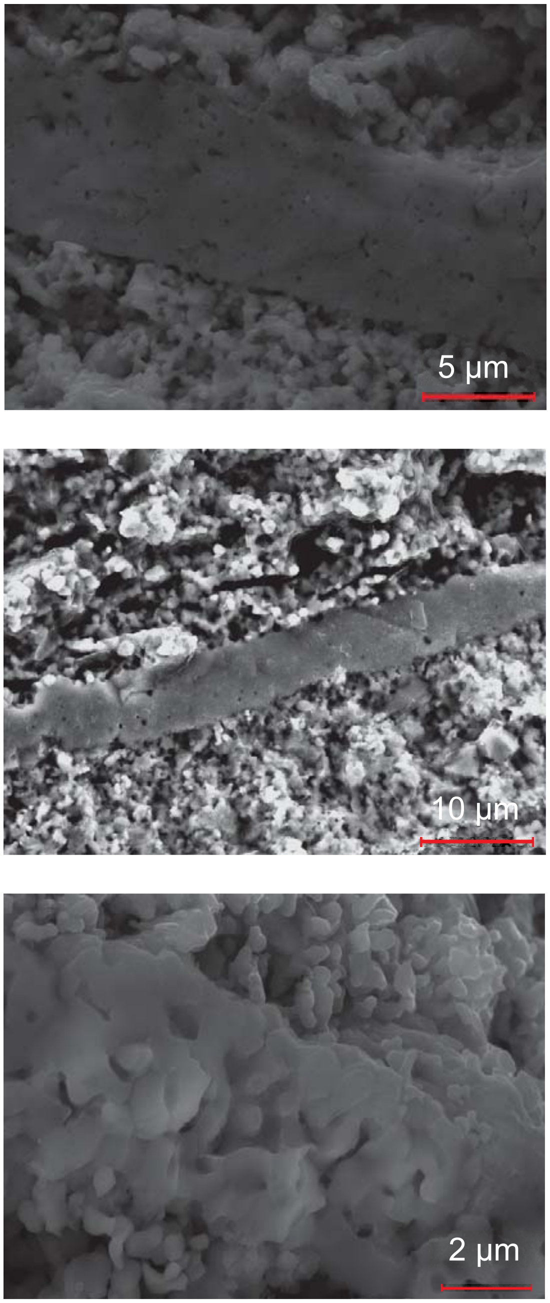

Figure 43: Micrographs are shown of fracture surfaces for the 3 highest power density SOFCs, in increasing power density at 800°C from top to bottom, 300 mW/cm^2, 0.81 OCV, 8 µm thick, 440 mW/cm^2, 7.8 µm thick, 1.03 OCV 520 mW/cm^2 0.7 OCV, 4.7 µm thick.

Overall, performance was found to correlate to electrolyte thickness, with a tradeoff of lower cell resistance as thickness decreased, accompanied with open circuit voltage loss due to gas permeation of the electrolyte porosity causing partial short circuiting of the electrochemical reaction.

Electrolytes under approximately 5 µm thick tended to have increased porosity, while thicker electrolytes converged towards densities of around 97%. These thin electrolytes could only be produced with suspensions containing acetic acid, due to the deposit adherence issues described in chapter 4. The thinnest functional electrolyte was produced from a deposition time of 30s and resulted in a 4.7 µm porous electrolyte. The difference in porosity versus deposit thickness can be seen by comparing the micrographs in Figure 44 of progressively thicker deposits. Please note that some of the greater thickness of the final deposit shown in Figure 44 is due to a substrate lamination defect, a void between laminate layers, which limited deposition on a portion of the substrate, effectively magnifying the current density on the defect free portions of the substrate and thus increasing deposition rate. The performance of these SOFCs are reported in Table 7. Ultimately, open circuit voltage loss due to electrolyte porosity necessitated a minimum thickness for high power density electrolytes of approximately 4-5 µm.

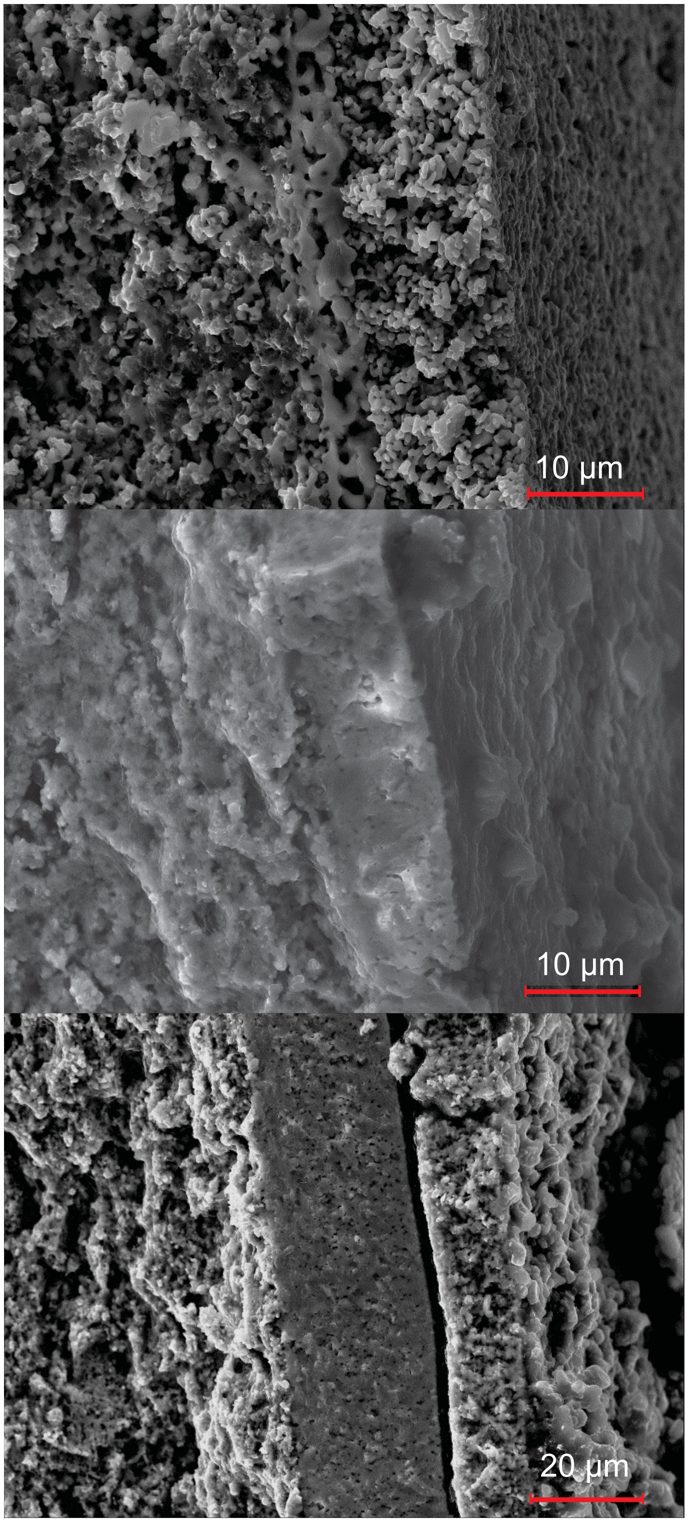

Figure 44: Micrographs are shown of progressively thicker deposits of 4.7, 10.4, and 27 μm YSZ electrolytes, with open circuit voltages of 0.8, 1, and 1.05 V respectively. These deposits were formed for 30s, 60s, and 10 minutes.

Table 7: A comparison is shown of EPD electrolyte thickness versus SOFC performance characteristics, at 800 °C, for deposits formed from 0.25 volume % 13 m^2/g YSZ, 1 weight % PEI, 8 g/L PVB, and 3 x 10^{-2} M acetic acid, in ethanol and sintered for 2 hours at 1400°C. Note, the 30 s deposit was only stable for the 900 °C test.

Deposition Time	Electrolyte Thickness (μm)	Open Circuit Voltage	Peak Power Density (mW/cm^2)	Total Interfacial Resistance ($\Omega \cdot cm^2$)
1 s	1.9	<0.1	n/a	n/a
30 s	4.7	0.8	200 @900 °C	0.39 @900 °C
60 s	10.4	1.0	190	2.55
10 min	27	1.05	75	3.15
10 min	14	1.03	150	1.67

The increased porosity of thin electrolytes is believed to be a side effect of the deposition mechanism, with the suggestion that the packing density increases initially with thickness towards a convergence point based on particle size distribution and the electrophoretic properties of the suspension. The driving forces of this initiation period appear to be the combined effect of the increasing voltage, at constant current deposition, needed to overcome the deposit resistance as well as the cumulative time under an applied voltage itself. What is known is that the packing density of deposits was uniform for deposits of >5 microns thick, and that only deposition times <60s produced such coatings. Over that time frame, voltage is not particularly stable, but is at its lowest. Particles in the deposit still have some mobility and under an applied voltage, the densest packing of particles represents the lowest energy state of the system. Also, during the initiation period, the concentration of particles near the electrode is increasing. Therefore, when both the driving force, the applied voltage, is increased and the amount of time is increased, packing density of deposits will increase towards optimal packing. This does not mean that more voltage or longer deposition time universally produce denser coatings, as each of these has a trade of with other suspension and deposition parameters, as previously discussed. However, in a stable operating deposition process, the key trait is that the particles and their packing coordination are not fixed at the moment of electrode contact, but evolve over the course of deposition.

In EPD deposits thicker than approximately 5 μm, it was found that performance of fuel cells produced thereof was not directly impacted by the processing parameters of acetic acid content, PEI content, PVB content, deposition current density, deposition voltage, or deposition time, but was only affected by the thickness of the resultant sintered coating and the presence of any cracking. While processing parameters do have an impact on deposition rate, deposit growth uniformity, and crack initiation, the density of sintered deposits showed minimal variation, based on polished and fracture cross section imagines. As the d_{90} of the particles is 1.8 μm, with the majority of particles close to the median particle size of 0.084 μm, deposits formed from these particles sinter well, with measured porosity likely to be from coalesced pores [84]. The sintered density could be further improved with a narrower particle size distribution, as shown by Sarkar et al. with 500 nm silica spheres [45]. The relative independence of SOFC performance to EPD processing parameters, within the range of uniform and crack free coatings, as well as the density uniformity between differing EPD parameters, supports the deposition mechanism of collapsing particle boundary layers upon approach to the growing deposit and the emphasis on deposition occurring primarily along the shortest conductive path relative to electric field strength. As particle boundary layers collapse from an initial state of high repulsion, denser particle packing is enabled, while the electric field strength pulls particles towards gaps or troughs between previously deposited particles, rather than allowing particles to permanently attach to whatever particle they initially contact. When this set of steps is not met, uniform coatings do not occur and thus EPD processing parameters can be optimized with concern focused primarily on achieving uniform crack free deposit buildup of minimal thickness.

5.3. Discussion of GDC/YSZ Bilayer Effectiveness

The YSZ/GDC bilayer electrolytes were developed to provide separation of the GDC from low partial pressure of oxygen, which induces electrical conductance, while taking advantage of the higher oxygen ion conductivity of GDC to facilitate improved intermediate temperature SOFC performance. Open circuit voltage measurements of thin YSZ electrolytes were used to design YSZ layers that were sufficient to protect the GDC from low partial pressures of oxygen, while being otherwise permeable so that the YSZ contributed minimally to cell ionic resistance. First, the findings from YSZ deposition were applied to GDC only deposition, with the discovery that the GDC deposited very similarly to the YSZ, except at a lower voltage, an average of 16-30 V, versus the 30-40 V of YSZ. A micrograph of a cross section from a GDC only deposition can be seen in

Figure 45. Note the similarity in microstructure to the YSZ deposits previously shown. As mentioned in chapter 4 and Figure 41, distinguishing the GDC and YSZ interfaces was difficult, even with EDS mapping. However, visually they were easily distinguished, as YSZ is white and GDC is peach in color, though this only sufficed for the top coat identification of the bilayer.

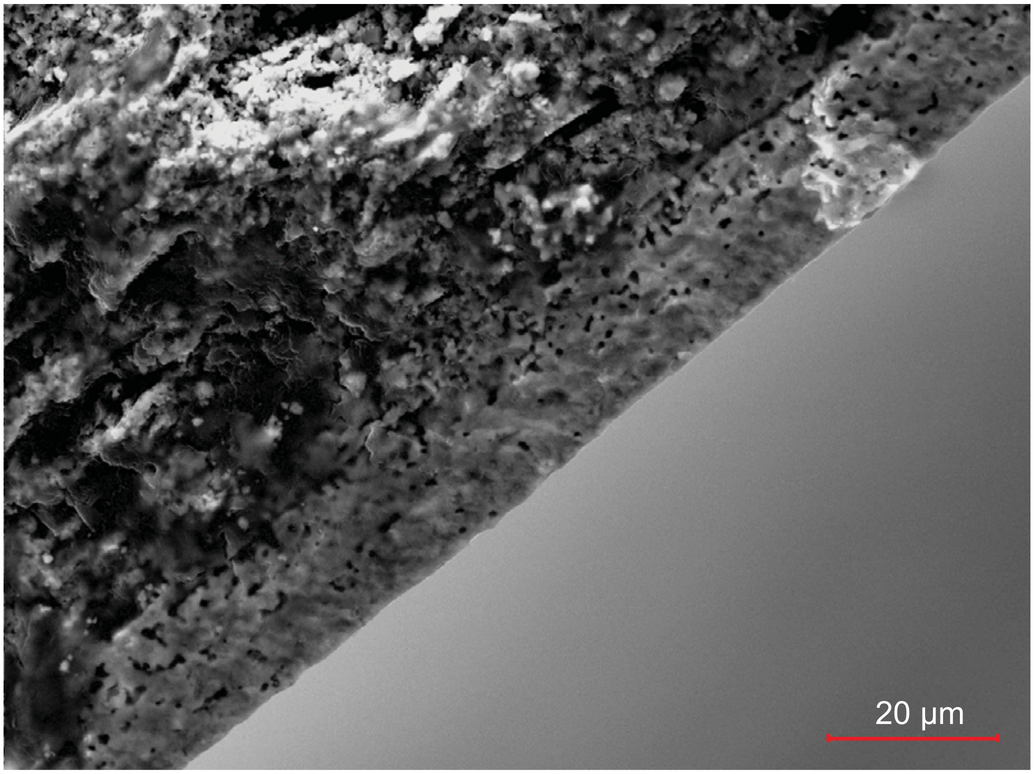

Figure 45: A micrograph is shown of a GDC deposit after a 1400 °C sinter for 2 hours. The deposit was formed from 0.25 vol. % GDC, 1 wt. % PEI, and 8 g/L PVB.

Additionally, the GDC had no adherence issues, with acetic acid addition instead having a negative impact on adherence. This led to multiple deposition methods being attempted to produce the YSZ/GDC bilayers, as the acetic acid content of the initial YSZ layer prevented subsequent deposition of GDC, while YSZ deposited without acetic acid required such thick coatings as to negate the purpose of the GDC. These deposition methods included sequential wet deposition of YSZ, then GDC, mixed composition suspension deposition, and finally the introduction of an intermediate 1000 °C bisque for 2 hours between YSZ deposition with acetic acid and GDC deposition. In Table 8, the deposits that formed functional cells are compared based on performances at 800 °C. The mixed composition suspensions were completely unsuccessful as SOFCs, while the sequential wet deposition proved unreliable, with the successful deposits limited by the necessary thickness of the YSZ layer. However, the intermediate bisque method allowed thinner YSZ layers and showed superior low temperature performance.

Table 8: An SOFC performance comparison at 800 °C of successful YSZ/GDC SOFCs is shown.

	Open Circuit Voltage	Peak Power Density (mW/cm^2)	Total Interfacial Resistance (Ω·cm^2)
5 minute YSZ – 10 minute GDC (no acetic acid)	0.95	350	0.68
2.5 minute YSZ – 5 minute GDC (no acetic acid)	0.75	240	0.34
60 s YSZ (3 x 10^{-2} M acetic acid) – bisque – 5 minute GDC	1.05	247	0.21

Ultimately, while YSZ/GDC bilayers were successfully fabricated, their performance, in absolute terms, did not exceed the performance of the YSZ electrolytes alone. However, the intermediate temperature performance of the optimized YSZ/GDC bilayers, relative to their high temperature performance, exceeded the YSZ electrolytes intermediate temperature performance relative to high temperature performance. Specifically, the optimized YSZ/GDC bilayer peak power density at 600 °C was 42 mW/cm^2, 17% of the 800 °C peak power density of 247 mW/cm^2. In comparison, the best performing YSZ electrolyte had a similar peak power density of 40 mW/cm^2 at 600 °C, but that was only 9% of the 800 °C peak power density of 440 mW/cm^2. For more detail, see Table 9 and Table 10.

Table 9: An SOFC performance versus temperature is shown for the highest performing stable SOFC, a 7.8 μm thick YSZ electrolyte deposited for 10 minutes at 0.47 mA/cm^2 from a suspension of 0.25 volume % 13 m^2/g YSZ, 1 weight % PEI, 8 g/L PVB, and 10^{-2} M acetic acid, in ethanol and sintered for 2 hours at 1400°C.

Temperature (°C)	Peak Power Density (mW/cm^2)	Total Interfacial Resistance (Ω·cm^2)
600	40	5.8
700	190	1.9
800	440	0.7
900	1050	0.35

Table 10: An SOFC performance versus temperature comparison for the best GDC/YSZ electrolyte is shown. The bilayer was formed of 0.25 vol. % 13m^2/g YSZ, 1 wt. % PEI, and 8 g/L PVB, 3 x 10^{-2} M acetic acid deposited for 60s, followed by a 1000 °C bisque for 2 hours, and finally a 5 minute deposition of 0.25 vol. % GDC, 1 wt. % PEI, and 8 g/L PVB. Note, at 500 °C, measurement quality was affected by high cell impedance, exceeding the testable frequency range of the equipment.

Temperature (°C)	Peak Power Density (mW/cm^2)	Total Interfacial Resistance (Ω·cm^2)
500	7	>60
600	42	5
700	120	0.72
800	247	0.21
900	480	0.09

5.4 Discussion of Sc-Nitrate Suspension Doping Effectiveness

While EDS measurements confirmed the presence of scandium in YSZ coatings created with scandium nitrate doped suspensions using both VLPSPS and EPD, only the VLPSPS electrolytes absorbed the scandium sufficiently to function as an electrolyte. The VLPSPS coatings were created at a time before the SOFC testing procedure had been refined to improve current density, but the open circuit voltage measurements were in line with un-doped YSZ electrolytes, while the admittedly low current densities measured were nonetheless greatest of all the VLPSPS electrolytes. EPD coatings produced with scandium nitrate doping were found to be electrically conductive during SOFC testing, as evidenced by their low open circuit voltage combined with low interfacial resistance, as shown in Table 11. This performance confirms that the scandium does not uniformly diffuse into the YSZ particles during sintering. Increasing the heat treatment temperature did correspond to a modest increase in performance, but with cells of this poor quality, comparisons are not reliable. However, it is reasonable to assume that longer and or higher temperature heat treatments would result in more scandium diffusion into the YSZ particles and improved performance. Another method of improvement would be to lower the initial suspension concentration, as the doping efficiency is as high as 54%, as discussed in chapter 4.

Table 11: An SOFC performance comparison at 900 °C of deposits formed with suspensions of 0.25 vol. % 13m^2/g YSZ, 1 w. % PEI, 8 g/L PVB, and 16 mole % Sc-nitrate, deposited 10 minutes is shown.

Heat Treatment	Open Circuit Voltage	Peak Power Density (mW/cm^2)	Total Interfacial Resistance (Ω·cm^2)
1400 °C – 2 hour	0.16	25	0.03
1500 °C – 2 hour	0.3	50	0.04

CHAPTER 6. CONCLUSIONS

This document has detailed significant findings made with respect to the emerging processes of very low pressure plasma spray (VLPPS) and suspensions plasma spray (SPS), here termed very low pressure suspension plasma spray (VLPSPS) when combined, as well as the competing and further developed process of electrophoretic deposition (EPD), which shares many capabilities and deposit characteristics with these two processes, when combined. These processing characteristics have been analyzed in terms of their efficacy in fabrication of compositionally controlled thin and pore free solid oxide fuel cell (SOFC) electrolytes with the potential of complex shape deposition. The key results from each of these subjects is reviewed in this chapter.

6.1 Process Efficacy and Coating Quality

6.1.1. Very Low Pressure Suspension Plasma Spray

The VLPSPS coating technology is still emerging with the capability to prepare coatings in thickness and density regimes not currently accessible with conventional thermal spray processes. By combining SPS with VLPPS, thin and pore free electrolytes of ideal composition for SOFCs are possible. By working at pressures as low as 320 Pa, energy partitioning in the plasma and its interaction with the surrounding chamber atmosphere was dramatically reduced. The result was a significant increase in plasma mean free path length and plasma velocity. This caused the plasma to remain coherent longer and deposit uniformly over larger areas, with a cylinder of relative uniform deposition approximately 15 cm in diameter and at least 15 cm in length at standoff distances beyond 109 cm. This uniform deposition volume increased dramatically with reduction in environmental pressure below 600 Pa, with sensitivity to even 5 Pa changes in pressure. The increased plasma volume also increases the total time particles are entrained in the high enthalpy plasma and consequently the amount of energy these particles absorb. The increased residence time in the plasma ensures dopants diffuse into the powder before reaching the substrate.

It has been shown in this research that compounds dissolved in the suspension (i.e. dopants) are incorporated into the coating during plasma spraying. Thus, it is possible to change the chemistry of the micron-sized powder during the short millisecond time the powder and dopant is in the hot spray plume. This means that it is possible to quickly and systematically change the composition of the sprayed SOFC electrolyte to optimize its oxygen-ion conductivity by simply adjusting the suspension composition. It also means that that an entire fuel cell could be created with a single piece of controlled atmosphere suspension plasma spray equipment, using both composition and porosity graded coatings to create each SOFC component in sequence. This coating control capability has the potential to significantly improve the state of the art in SOFC production, but requires further investigation to reach that point. Important steps in that direction would be to have an operational deposition standoff distance window beyond 125 cm and the capability to operate in the very low pressure regime, while maintaining constant chamber pressure. Also, considering the significant change in plasma expansion observed below 300 Pa, it may be preferable to define very low pressure plasma spray along this more restrictive range.

The deposition efficiency was calculated based on the coating thickness, suspension powder loading, feed rate, feed time, and the approximate deposition area of the plasma plume, a circle of 15 cm diameter, which accounted to be <10%. Additionally of note is that loose un-adhered powder deposits every surface of the chamber after running the process and particularly collects in the shrouded area around the edge of the substrate. The particle size distribution, shown in Figure 11, of the 40 m^2/g YSZ VLPSPS powder indicates that approximately 15% are between 0.5-2 microns, with the majority being split between 35% with a mean of 0.1 microns and 50% with a mean of 7. It is assumed the largest particles are primarily agglomerates of the smaller particles, which is supported by their absence from the coatings and the shroud. As was shown in Figure 24, the shrouded area tends to contain many smaller particles, while the deposited surface is made primarily of particles around 1 micron and neither surface contains indication of splat-like shapes.

VLPSPS deposition is particle size selective, in a similar fashion to atmospheric SPS. As particle size goes down, the degree of flow with the carrier gas/plasma increases as momentum vs. surface area decreases. Any moving fluid encountering a surface generates a boundary layer, meaning any particle without sufficient momentum to overcome gas flow will not deposit. Also, the pressure differential between the chamber and the plasma means gas is continually flowing out of the plume along its standoff distance. This selectivity is increased when there is insufficient power to deposit fully molten particles, with selectivity against smaller particle size decreasing with standoff distance as the substrate boundary layer weakens and selectivity against large particle size based on the gun power and suspension medium. Thus, the smallest particles are continually eliminated from the plume via thermophoresis and the continued expansion of the plasma into the vacuum chamber, while the largest particles may never melt. Those particles that remain at high standoff distances are at the lowest temperature of the overall gun to substrate particle stream, but sufficient to both penetrate the boundary layer and adhere to the substrate. This does allow for smaller particle agglomerates to melt and combine, but they would have to be mostly re-solidified by the point of deposition, based on the observed microstructures.

6.1.2. Electrophoretic Deposition

Electrophoretic deposition enables cost effective fabrication of thin and pore free electrolytes for solid oxide fuel cells, with the capability of deposition on complex shapes as well as a measure of controlled texture via patterned deposition through electrode application. Additionally, it was shown that metal salts could be incorporated into deposits at proportions greater than the relative volume of salt to the suspension, thus indicating the interaction of these metal salts with the diffuse boundary layer around depositing particles and representing an efficient way to modify deposit composition. However, in the heat treatments explored, the resultant scandia content was found to not diffuse thoroughly into the YSZ particles. Further development of the process, both in heat treatment and in applying the process to higher specific surface area deposits should improve the diffusion of dopants.

The suspension with the greatest reproducibility of uniform and well adhered deposits from this study consisted of 0.25 vol. % YSZ, with a specific surface area of 13 m^2/g, 1 weight % PEI, 8 g/L PVB, and 3x10^{-2} M acetic acid deposited at 0.47 mA/cm^2 at 10 mm electrode separation. Sintered deposits reached 97% density, but coalesced pores were present after sintering. In addressing deposit cracking, the key suspension properties were found to be the specific surface area of the particles and the presence of the binder polyvinyl butyral (PVB). TGA revealed the as deposited coating is approximately 97.5 weight % YSZ, which amounts to 88 vol. % YSZ, not counting porosity, with the remainder being a combination of PEI and PVB. Assuming a standard drying shrinkage of 10-15% and a particle packing density of 60%, this means the combined PEI and PVB content in the liquid phase of the growing deposit is between 14 -16 vol. % and 18 -19 wt. %, which represents a very large increase over the combined 2 wt. % they represented in the bulk suspension. This relative composition difference from the suspension to the deposit represents the degree of interaction between the PEI, PVB, and YSZ during deposition, as well as the suspension constituent depletion rate. With further study, this suspension constituent depletion rate could be characterized such that it could be compensated for with the periodic or continual addition of a second, more concentrated, suspension. This method could be used to eliminate waste of depleted suspensions and facilitate steady state operation of EPD equipment.

The TGA and observed effects of acetic acid content point toward deposition caused by changing concentration of double boundary layer constituents at the electrode. The TGA showed the relative increase in double boundary layer constituents from the bulk suspension to the growing deposit, while acetic acid addition in YSZ suspensions reduced the initial deposit formation time and increased the adhesion thereof. It is likely that the increased concentration of acetic acid at the electrode degrades the local stability of the YSZ, causing flocculation, deposition, and the formation of well adhered deposits.

6.2. Solid Oxide Fuel Cell Performance and Processing Relationships

The open circuit voltage of VLPSPS and EPD electrolyte SOFCs was found to be dependent on the electrolyte thickness due to the porosity and permeability of the deposits. With VLPSPS, the highest OCV at 800 °C achieved was 0.93 V, from the thickest YSZ coating, ~11 μm. With EPD, the highest OCV at 800 °C was 1.05 V, for a ~27 μm YSZ coating, though EPD coatings commonly exceeded 1 V when as thin as 7.8 μm. This thickness relationship was attributed to porosity in the coatings allowing for permeability of the electrolytes at lower thicknesses. These OCV measurements and analysis of the microstructures show that the sintered EPD coatings have less pores than the VLPSPS coatings, but the

VLPSPS coatings approach the packing density of the EPD coatings while still in the as-deposited state.

While EDS measurements confirmed the presence of scandium in YSZ coatings created with scandium nitrate doped suspensions using both VLPSPS and EPD, only the VLPSPS electrolytes absorbed the scandium sufficiently to function as an electrolyte. The VLPSPS coatings were created at a time before the SOFC testing procedure had been refined to improve current density, but the open circuit voltage measurements were in line with un-doped YSZ electrolytes, while the low current densities measured were nonetheless greatest of all the VLPSPS electrolytes. EPD coatings produced with scandium nitrate doping were found to be electrically conductive during SOFC testing. Their performance in a SOFC confirmed that the scandium did not uniformly diffuse into the YSZ particles during sintering. Increasing the heat treatment temperature did correspond to a modest increase in performance, but the overall poor cell quality limits the significance. However, it is reasonable to assume that longer and or higher temperature heat treatments would result in more scandium diffusion into the YSZ particles and improved performance.

YSZ electrolyte coatings produced using electrophoretic deposition performed comparably to similar coatings reported by Hosomi et al. [55] and Besra et al. [54]. The highest stable power density achieved was approximately 440 mW/cm^2 at 800 °C for a cell consisting of a NiO/YSZ anode, screen printed LSCF cathode, and a 7.8 μm thick YSZ electrolyte deposited for 10 minutes at 0.47 mA/cm^2 from a suspension of 0.25 volume % 13 m^2/g YSZ, 1 weight % PEI, 8 g/L

PVB, and 10^{-2} M acetic acid, in ethanol and sintered for 2 hours at 1400°C. At 800 °C, the total interfacial resistance of this cell, as measured via impedance spectroscopy, was 0.7 $\Omega \cdot cm^2$.

YSZ/GDC bilayers were successfully fabricated, though their performance, in absolute terms, did not exceed the performance of the YSZ electrolytes alone. However, the intermediate temperature performance of the optimized YSZ/GDC bilayers, relative to their high temperature performance, exceeded the YSZ electrolytes intermediate temperature performance relative to high temperature performance. Specifically, the optimized YSZ/GDC bilayer peak power density at 600 °C was 42 mW/cm^2, 17% of the 800 °C peak power density of 247 mW/cm^2. In comparison, the best performing YSZ electrolyte had a similar peak power density of 40 mW/cm^2 at 600 °C, but that was only 9% of the 800 °C peak power density of 440 mW/cm^2.

While this research was unable to thoroughly investigate the SOFC performance of VLPSPS electrolytes, the similarities in microstructure between the sintered EPD electrolytes and the as-sprayed VLPSPS electrolytes suggests the potential performance of VLPSPS electrolytes. Areas for further investigation of VLPSPS should focus on utilizing suspensions with smaller particle size, higher plasma gun power, and lower stable chamber pressures, ideally <300 Pa.

LIST OF REFERENCES

LIST OF REFERENCES

1. Fuel Cell Handbook (Seventh Edition), *Solid oxide fuel cells*, EG&G Technical Services, U.S. Department of Energy, Office of Fossil Energy, National Energy Technology Laboratory, 7-1 - 7-45, 2004.

2. Goodenough, J., *Oxide-ion electrolytes*, Annual Review of Materials Research, 33 (2003) 91-128.

3. Srivastava, P., Quach, T., Duan, Y., Donelson, R., Jiang, S., Ciacchi, F., Badwal, S., *Electrode supported solid oxide fuel cells: electrolyte films prepared by DC magnetron sputtering*, Solid State Ionics 99 (l997) 311-319.

4. Y.J. Leng, S.H. Chan, K.A. Khor, S.P. Jiang, *Performance evaluation of anode supported solid oxide fuel, cells with thin YSZ electrolyte*, International Journal of Hydrogen Energy 29 (2004) 1025-1033.

5. Bieberle-Hutter, A., et al., *A micro-solid oxide fuel cell system as battery replacement*, Journal of Power Sources 177 (2008) 123-130.

6. U.S. Department of Energy. *FCT Fuel Cells: Types of Fuel Cells.* 2009. Retrieved from http://www1.eere.energy.gov/hydrogenandfuelcells/fuelcells/fc_types.html

7. Brown, J., Solid Oxide Fuel Cells, *High conductivity solid ionic conductors*, Editor Takehiko Takahashi, (1989) 630-663.

8. Mogensen, M., et al, *Factors controlling the oxide ion conductivity of fluorite and perovskite structured oxides*, Solid State Ionics 174 (2004) 279-286.

9. Kharton, V., et al., *Perovskite-type oxides for high-temperature oxygen separation membranes*, Journal Membrane Science 163 (2) (1999) 307.

10. Elshof, J., Bouwmeester, H., Verweij, H., *Oxygen transport through La1−xSrxFeO3-δ membranes II. Permeation in air/CO, CO2 gradients*, Solid State Ionics 89 (1-2) (1996) 81.

11. Teraoka, Y., Zhang, H., Furukawa, S.,Yamazoe, N., Oxygen *permeation through perovskite-type oxides*, Chemistry Letters 11 (1985) 1743

12. Badwal, S., *Zirconia-based solid electrolytes: microstructure, stability and ionic conductivity*, Solid State Ionics 52 (1992) 23-32.

13. Guo, X, *Can We Achieve Significantly Higher Ionic Conductivity in Nanostructured Zirconia*, Scripta Materialia, 65(2), July 2011, pp. 96-101.

14. Jiang, S., *A review of wet impregnation: An alternative method for the fabrication of high performance and nano-structured electrodes of solid oxide fuel cells*, Materials Science and Engineering A, 418 (2006) 199-210.

15. Smith, M; Hall, A.; Fleetwood, J.; Meyer, P. *Very Low Pressure Plasma Spray - A Review of an Emerging Technology in the Thermal Spray Community*, Coatings, 1 (2011) 117-132.

16. Singh, P; Minh, N, *Solid oxide fuel Cells: technology status*, International Journal of Applied Ceramics Technology, 1 (2004) 5-15.

17. T. Tsai, E. Perry, S. Bernett, *Low-temperature solid-oxide fuel cells utilizing thin bilayer electrolytes*, Journal of Electrochemical Society 144 (1997) L130-L132.

18. Muecke, U., et al., *Electrochemical performance of nanocrystalline nickel/gadolinia-doped ceria thin film anodes for solid oxide fuel cells*, Solid State Ionics 178 (2008) 1762-1768.

19. Li, P. and Chen, I., *Effect of Dopants on Zirconia Stabilization-An X-ray Absorption Study: I, Trivalent Dopants*, J. Am. Ceram. Soc., 77(1), 1994, pp. 118-128.

20. Argyriou, D., Howard, C., Lathabai, S., *Further observations of an orthorhombic zirconia in magnesia-partially stabilized zirconia*, in: S.P.S. Badwal, M.J. Bannister, R.H.J. Hannink (Eds.), Science and Technology of Zirconia V, A Technomic Publishing Company, Pennsylvania, 1993, 69.

21. Dorier, J.; Gindrat, M.; Hollenstein, Ch.; Loch, M.; Refke, A.; Barbezat, G. *Plasma jet properties in a new spraying process at low pressure for large area thin film deposition*, In Proceedings of the 2001 International Thermal Spray Conference, Singapore, 28–30 May 2001, 1-6.

22. Jodoin, B.; Gindrat, M.; Dorier, J.L.; Hollenstein, C.; Lcoh, M.; Barbezat, G. *Modeling and diagnostics of a supersonic DC plasma jet expanding at low pressure*. In Proceedings of the International Thermal Spray Conference, Essen, Germany, March 2002, 716-720.

23. Gindrat, M.; Dorier, J.-L; Hollenstein, Ch.; Loch, M.; Refke, A.; Salito, A.; Barbezat, G. *Effect of specific operation conditions on the properties of LPPS plasma jets expanding at low pressure*. In Proceedings of the International Thermal Spray Conference, Essen, Germany, March 2002, 459-464.

24. Bolot, R.; Klein, D.; Coddet, C. *Design of a nozzle extension for thermal spray under very low pressure conditions*. In Proceedings of the International Thermal Spray Conference, Osaka, Japan, May 2004, 574-579.

25. Kingswell, R.; Scott, K.T.; Wassel, L.L. *Optimizing the vacuum plasma spray deposition of metal, ceramic, and cermet coatings using designed experiments*. J. Therm. Spray Technol. 1993, *2*, 179-185.

26. Bolot, R.; Sokolov, D.; Klein, D.; Coddet, C. *Nozzle developments for thermal spray at very low pressure*. J. Therm. Spray Technol. 2006, *15*, 827-833.

27. Siegert, R., *A Novel Process for the Liquid Feedstock Plasma Spray of Ceramic Coatings with Nanostructural Features*, Doctoral Thesis, Institut fur Werkstoffe und Verfahren der Energietechnik, 2005.

28. VanEvery, K., *Development and Evaluation of Suspension Plasma Sprayed Yttria Stabilized Zirconia Coatings as Thermal Barriers*, Doctoral Thesis, Purdue University, 2009.

29. Chen, Z., Trice, R., *Air-plasma spraying colloidal solutions of nanosized ceramic powders*, Journal of Materials Science, 39, 2004, 4171-78.]

30. Delbos, C., et al., *Phenomena Involved in Suspension Plasma Spraying, Part 2: Zirconia Particle Treatment and Coating Formation*, Plasma Chemistry and Plasma Processing, 26, (2006) 393-414.

31. Berghaus, J., Bouaricha, S., Legoux, J., Moreau, C., *Injection conditions and in-flight particle states in suspension plasma spraying of alumina and zirconia nano-ceramics*, proceedings of the International Thermal Spray Conference, May 2-4, 2005, Basel, Switzerland.

32. Berghaus J., Bouaricha, S., Legoux, J., Moreau, C., Chraska, T., *Suspension plasma spraying of nano-cermics using an axial injection torch*, proceedings of the International Thermal Spray Conference, May 2-4, 2005, Basel, Switzerland.

33. Chen, Z., Trice, R., “Air-plasma spraying colloidal solutions of nanosized ceramic powders,” *Journal of Materials Science*, 39, (2004) 4171-78.

34. Fazilleau, J., et al, *Phenomena Involved in Suspension Plasma Spraying Part 1: Suspension Injection and Behavior*, Plasma Chemistry and Plasma Processing, 26, (2006) 371–391.

35. Siegert, R., *A Novel Process for the Liquid Feedstock Plasma Spray of Ceramic Coatings with Nanostructural Features*, Doctoral Thesis, Institut fur Werkstoffe und Verfahren der Energietechnik, 2005.

36. Liu, H., *DROPLETS: Fundamentals and Applications*, Noyes Publications: Park Ridge, New Jersey, Copyright 2000.

37. Fauchais, P., *Understanding plasma spraying*, Journal of Physics D: Applied Physics, 37, (2004). 86-108

38. Sato, N., Kawachi, M., Noto, K., Yoshimoto, N., Yoshizawa, M., *Effect of particle size reduction on crack formation in electrophoretically deposited YBCO films*, Physica C., 2001, 357–360, 1019–22.

39. Heavens, N., *Electrophoretic deposition as a processing route for ceramics,* In: Binner, G.P.(ed.) Advanced ceramic processing and Technology, 1, Noyes Publications, Park Ridge, 1990.

40. Hamaker, H., *Formation of deposition by electrophoresis*, Trans. Faraday Soc., 36, 1940, 279–287.

41. Biesheuvel, P., Verweij, H., *Theory of cast formation in electrophoretic deposition*, J. Am. Ceram. Soc. 82, 6, 1999, 1451–55.

42. Avgustinik, A., Vigdergauz, V., Zharavlev, G., *Electrophoretic deposition of ceramic masses from suspension and calculation of deposit yields*, J. Appl. Chem., 35, 10, 1962, 2175–80.

43. Ishihara, T., Shimise, K., Kudo, T., Nishiguchi, H., Akbay, T., Takita, Y., *Preparation of Yttria-stabilised zirconia thin-films on strontium doped LaMnO3 cathode substrate via Electrophoretic deposition for solid oxide fuel cells*, J. Am. Ceram. Soc., 83, 8, 2000, 1921–27.

44. Chen, F., Liu, M., *Preparation of yttria-stabilised zirconia (YSZ) films on La0.85Sr0.15MnO3(LSM) and LSM-YSZ substrate using an electrophoretic deposition (EPD) process*., J. Eur.Ceram. Soc., 21, 2001, 127–134.

45. Sarkar, P., De, D., Yamashita, K., Nicholson, P., Umegaki, T., *Mimicking nanometer atomic processes on a micrometer scale via electrophoretic deposition*, J. Am. Ceram. Soc., 83, 2000, 1399–1401.

46. De, D., Nicholson, P., *Role of Ionic Depletion in Deposition during Electrophoretic Deposition*, J. Am. Ceram. Soc., 83 (1999) 3031-36.

47. Besra, L., Liu, M., *A review on fundamental and applications of Electrophoretic deposition*, Prog. Mater. Sci. 52, 1, 2007, 1–61.

48. Ferrari, B., Moreno, R., *Electrophoretic deposition of aqueous alumina slip*, J. Eur. Ceram. Soc., 1997, 17, 549–556.

49. Ferrari, B., Moreno, R., *The conductivity of aqueous Al2O3 slips for electrophoretic deposition*, Mater. Lett., 1996, 28, 353–355.

50. Wang, Y., Leu, I., Hon, M., *Kinetics of electrophoretic deposition for nanocryatalline zinc oxide coatings*, J. Am. Ceram. Soc., 2004, 87, 1, 84–88.

51. Ciou, S., Fung, K., Chiang, K., *The mathematical expression for kinetics of electrophoretic deposition and the effects of applied voltage*, J. Power Sources, 2007, 172, 358-362.

52. Sarkar, P., De, D., Uchikochi, T., Besra, L., *Electrophoretic Deposition (EPD): Fundamentals and Novel Applications in Fabrication of Advanced Ceramic Microstructures*, In Electrophoretic Deposition of Nanomaterials, Nanostructure Science and Technology, 2012, 181-215.

53. Besra, L., Lie, M., *A review of fundamentals and applications of electrophoretic deposition (EPD)*, Progress in Materials Science, 52, 2007, 1-61.

54. Besra, L., Compson, C., Liu, M., *Electrophoretic deposition on non-conducting substrates: the case of YSZ film on NiO-YSZ composite substrates for solid oxide fuel cell application*, Journal of Power Sources, 173, 2007, 130-136.

55. Hosomi, T., Matsuda, M., Myake, M., *Electrophoretic deposition for fabrication of YSZ electrolyte film on non-conducting porous NiO-YSZ composite substrate for intermediate temperature SOFC*, Journal of European Ceramic Society, 27, 2007, 173-178.

56. Krueger, H., Knote, A., Schindler, U., Kern, H., Boccaccini, A., *Composite ceramic metal coatings by means of combined electrophoretic deposition*, J. Mater. Sci., 2004, 39, 839–844.

57. Fukada, Y., Nagarajan, N., Mekky, W., Bao, Y., Kim, H., Nicholson, P., *Electrophoretic deposition-mechanisms, myths and materials*, J. Mater. Sci, 2004, 39, 787-801.

58. Minh, N., Takahashi, T., *Anode*, Science and Technology of Ceramic Fuel Cell Cells, Elsevier, Amsterdam (1995) 147-164.

59. Twigg, M., Catalyst Handbook, 2nd edn, Manson Publishing, London, 1996.

60. Rostrup-Nielsen, J., in: J.M. Anderson, M. Boudart (Eds),Catalysis Science and Technology, vol. 5, Springer Verlag, Berlin, 1984.

61. Ivers-Tiffée, E., Virkar, A., *Electrode polarizations* in: S.C. Singhal, K. Kendall (Eds.), High Temperature Solid Oxide Fuel Cells, Elsevier, (2003) 230-257.

62. Anguoa, F., *Thin Film Mixed Conducting Cathodes for Intermediate Temperature Solid Oxide Fuel Cells*, Doctoral Thesis, Purdue University, 2010.

63. Kronig, R., Physik Zeitschrift, 30 (1929) 521.

64. Kramers, H., Physik Zeitschrift, 30 (1929) 522.

65. Heaviside, O., *Electricity*, New York and London: Macmillan and co, 2 (1850-1925)

66. Song, H., Macdonald, D., *Photoelectrochemical impedance spectroscopy*, Journal of the Electrochemical Society 138 (5) (1991) 1408-1410.

67. Boukamp, B., *Electrochemical impedance spectroscopy in solid state ionics:recent advances*, Solid State Ionics 169 (2004) 65-73.

68. Urquidi-Macdonald, M., Real, S., Macdonald, J., *Applications of Kramers-Kronig transforms in the analysis of electrochemical impedance data: III. Stability and linearity*, Electrochimica Acta 35 (1990) 1483.

69. Macdonald, D., *Reflections on the history of electrochemical impedance spectroscopy*, Electrochimica Acta 51 (2006) 1376-1388

70. Zhitomirsky, I., Gal-or, L., *Electrophoretic deposition of hydroxyapatite,* J. Mater. Sci: Mater. Med., 1997, 8, 213–219.

71. Basu, R., Randall, C., Mayo, M., *Fabrication of dense zirconia electrolyte films for tubular solid oxide fuel cells by electrophoretic deposition*, J. Am. Ceram. Soc., 2001, 84, 1, 33–40.

72. Vandeperre, L., Van Der Biest, O., Clegg, W., *Silicon carbide laminates with carbon interlayers by electrophoretic deposition*, Key Eng. Mater., 1, 1997, 127–131.

73. Sarkar, P., Nicholson, P*., Electrophoretic deposition (EPD): Mechanisms, Kinetics and Applications to Ceramics*, J. Am. Ceram. Soc., 79, 1996, 1987–2002.

74. Powers, R. *The electrophoretic forming of beta-alumina ceramic. J Electrochem Soc.*, 1975, 122, 482–486.

75. Mizuguchi, J., Sumi, K., Muchi, T., *A Highly Stable Non-aqueous Suspension for the Electrophoretic Deposition of Powdered Substances*. J. Electrochem. Soc., 130, (1983) 1819–25.

76. Zarbov, M., Schuster, I., Gal-Or, L., *Methodology for selection of charging agents for electrophoretic deposition of ceramic particles*, In: Proc. of the International symposium on Electrophoretic deposition: Fundamentals and applications, 2002–21, The electrochemical society Inc, Pennington, USA, 2002.

77. Gauckler, L., Godickemeier, M., Schneider, D., *Nonstoichiometry and defect chemistry of ceria solid solutions*, Journal of Electroceramics 1 (1997) 165-172.

78. Riess, I., Godickemeier, M., Gauckler, L., *Characterization of solid oxide fuel cells based on solid electrolytes or mixed ionic electronic conductors*, Solid State Ionics 90 (1996) 91-104.

79. Riess, I., *Mixed ionic-electronic conductors-material properties and applications*, Solid State Ionics 157 (2003) 1-17.

80. Steele, B., *Oxygen transport and exchange in oxide ceramics*, Journal of Power Sources, 49 (1994) 1-14.

81. Atkinson, A., *Chemically-induced stresses in gadolinium-doped ceria solid oxide fuel cell electrolytes*, Solid State Ionics 95 (1997) 249-258.

82. X.G. Zhang , D.F. Yang, , S. Nikum, C.D. Petit, R. Hui, R. Maric, D. Ghosh, *Sm0.5Sr0.5CoO3 + Sm0.2Ce0.8O1.9 composite cathode for cermet supported thin Sm0.2Ce0.8O1.9 electrolyte SOFC operating below 600°C*, Journal of Power Sources 161, Issue 1, (2006) 301-307.

83. Q.L. Liu, K.A. Khor, S.H. Chan, X.J. Chen, *Low temperature solid oxide fuel cells with pulsed laser deposited bi-layer electrolyte*, Journal of Power Sources 164 (2007) 182-188.

84. Kellet, B., Lange, F., *Thermodynamics of densification: I, sintering of simple particle arrays, equilibruim configurations, pore stability, and shrinkage*, J. Am. Ceram. Soc. 72, 1989, 725–734

VITA

VITA

James Fleetwood

Graduate School, Purdue University

Education

B.S., Materials Science & Engineering, 2009, Purdue University, West Lafayette, Indiana

Ph.D., Materials Engineering, 2014, Purdue University, West Lafayette, Indiana

Research Interests & Motivations

Powder Processing, Thermal Spray, Direct Laser Metal Deposition, Kinetics, & insatiable curiosity